AD-A053 159 AIL DEER PARK N Y F/G 4/1
IHR (INFRARED HETERODYNE RADIOMETER) FOR LOW ALTITUDE TEMPERATU--ETC(U)
MAR 78 I RUBINSTEIN N00014-76-C-0721
UNCLASSIFIED AIL-C618-2 NL

| OF |
AD
A053159

END
DATE
FILMED
6-78
DDC

IHR FOR LOW ALTITUDE TEMPERATURE PROFILE RETRIEVAL

FINAL REPORT

by

I. RUBINSTEIN

AIL REPORT NO. C618-2

MARCH 1978

PREPARED UNDER CONTRACT N00014-76-C-0721

OFFICE OF NAVAL RESEARCH

WASHINGTON, D.C.

AIL a division of CUTLER-HAMMER
DEER PARK, LONG ISLAND, NEW YORK 11729

IHR FOR LOW ALTITUDE TEMPERATURE PROFILE RETRIEVAL

FINAL REPORT

by

I. RUBINSTEIN

AIL REPORT NO. C618-2

TASK NO. NR211-203/4-01-77 (465)

MARCH 1978

PREPARED UNDER CONTRACT N00014-76-C-0721

OFFICE OF NAVAL RESEARCH

WASHINGTON, D.C.

AIL a division of CUTLER-HAMMER

DEER PARK, LONG ISLAND, NEW YORK 11729

Unclassified

SECURITY CLASSIFICATION OF THIS PAGE (When Data Entered)

REPORT DOCUMENTATION PAGE

READ INSTRUCTIONS BEFORE COMPLETING FORM

1. REPORT NUMBER: C618-2	2. GOVT ACCESSION NO.
3. RECIPIENT'S CATALOG NUMBER	
4. TITLE (and Subtitle): IHR (Infrared Heterodyne Radiometer) for Low Altitude Temperature Profile Retrieval.	5. TYPE OF REPORT & PERIOD COVERED: Final rept. Apr 1976-Mar 1978,
6. PERFORMING ORG. REPORT NUMBER	
7. AUTHOR(s): I. Rubinstein	8. CONTRACT OR GRANT NUMBER(s): N00014-76-C-0721
9. PERFORMING ORGANIZATION NAME AND ADDRESS: AIL Division, Cutler-Hammer, Deer Park, New York 11729	10. PROGRAM ELEMENT, PROJECT, TASK AREA & WORK UNIT NUMBERS
11. CONTROLLING OFFICE NAME AND ADDRESS: Office of Naval Research, 800 N. Quincy Street, Arlington, Virginia 22217	12. REPORT DATE: Mar 1978
	13. NUMBER OF PAGES: 56p.
14. MONITORING AGENCY NAME & ADDRESS (if different from Controlling Office): AIL-C618-2	15. SECURITY CLASS. (of this report): Unclassified
	15a. DECLASSIFICATION/DOWNGRADING SCHEDULE

16. DISTRIBUTION STATEMENT (of this Report)

DISTRIBUTION STATEMENT A
Approved for public release;
Distribution Unlimited

17. DISTRIBUTION STATEMENT (of the abstract entered in Block 20, if different from Report)

18. SUPPLEMENTARY NOTES

19. KEY WORDS (Continue on reverse side if necessary and identify by block number)

Infrared - Radiometer - Temperature - Retrieval
Index of Refraction, Atmospheric Variation

20. ABSTRACT (Continue on reverse side if necessary and identify by block number)

A technique for obtaining accurate temperature and humidity profiles with a grazing-angle up-looking radiometer, for the purpose of assessing index of refraction variations in the atmosphere has been investigated. The profiling technique is based on information retrievals which are obtained from difference-kernel functions generated from pairs of high spectral resolution radiometric channels. Spatially selective information → next page

DD FORM 1 JAN 73 1473 EDITION OF 1 NOV 65 IS OBSOLETE

SECURITY CLASSIFICATION OF THIS PAGE (When Data Entered)

404 967 JOB

ABSTRACT (continued)

can be generated from such functions with the required accuracy for retrieving temperature and humidity gradients at the lower altitude atmospheric levels.

A retrieval of an assumed double inverted temperature profile in the lower atmosphere, using three and four differential kernel information channels of CO_2 signature emission in the 13 μm region, has been simulated on a computer. The retrieval is based on iterative solutions of the radiative transfer equation and requires no apriori statistical knowledge of the atmospheric temperature profile. Temperature inversions at 375 and 750 meters, assumed for the selected atmospheric model, were reproduced in the simulated retrievals.

Results of an analysis on sensitivity limits, achievable with the coherent Infrared Heterodyne Radiometer (IHR) and the Fabry-Perot Etalon (FPE) spectro-radiometers show the FPE system as potentially superior in performance. A basic FPE spectroscopic configuration required to implement the technique is briefly outlined.

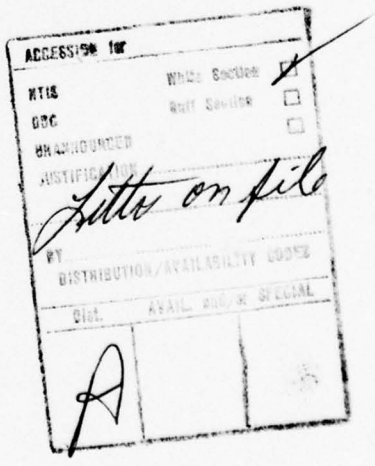

TABLE OF CONTENTS

LIST OF ILLUSTRATIONS

1.0 INTRODUCTION AND SUMMARY

This is a Final Report on Contract N00014-76-C-0721 entitled "IHR Low Altitude Temperature Profile Retrieval." The program is aimed at the development of radiometric techniques for the remote measurement of atmospheric vertical and slant path temperature and humidity distribution. The retrieved profiles are expected to be instrumental in decreasing the errors in measured target position resulting from refraction index gradients along an atmospheric propagation path.

Remote profile measurements of temperature and atmospheric gaseous constituents have been previously implemented by radiometric measurement of the upwelling radiance using instruments mounted on aircraft, satellite and balloon platforms (References 1 and 2). Unfortunately, altitude profile resolution obtainable with similar techniques when applied to up-looking sensors is inherently poor due to erratic (non-peaked) responses of the kernel (weighting) functions associated with downwelling radiation. The information thus obtained lacks sufficient detail to retrieve sharp gradients of temperature and humidity in the lower atmosphere which grossly affect local variations of refractive index.

An alternate technique for obtaining more accurate temperature and humidity profiles with a grazing-angle up-looking radiometer has been investigated and is discussed in detail in this report. The profiling technique is based on measuring radiation from pairs of rotational transition absorption lines characteristic of abundant

gases (such as CO_2) in the atmosphere. The technique enables the generation of difference-kernel functions which are well suited to the task. Spatially selective information thus generated may be utilized for high accuracy retrievals of temperature and humidity gradients at the lower altitude atmospheric levels such as within the Marine Boundary Layer.

Retrievals of a double-inverted temperature profile using the differential kernel method in the lower atmosphere have been simulated on a computer. For this effort the 13 μm CO_2 band is used. The model profile consisted of a double inversion at 375 meters and at 750 meters above the ocean surface. An iterative method for solutions of the radiative transfer equations, requiring no apriori statistical information on atmospheric parameters was used for profile retrieval. The general methodology of the simulated retrieval process is discussed in the report.

A profile retrieval based on three information channels was first simulated. The retrieved profile obtained, clearly reproduces the two inversions, however, the fidelity of the temperature gradient is somewhat poor at the lower altitude levels.

A second profile retrieval based on four information channels, with higher spatial selectivity kernels near ground level was then implemented. The resulting retrieval is in good agreement with the actual temperature distribution along the assumed slant path.

Two spectro-radiometric techniques, suitable for high spectral resolution remote sensing applications, were investigated on the program; namely, Infrared Heterodyne Radiometry (IHR) and Fabry-Perot Etalon (FPE) spectroscopy. A sensitivity analysis has been performed so as to assess the performance limits achievable with each radiometric type. The results of the analysis show the FPE to be superior in performance, primarily due to its higher optical throughput. As shown in this report, reasonably high signal-to-noise ratios (SNR) are potentially achievable with an FPE system. Basic spectroscopic techniques for achieving high spectral resolution using FPE configurations are briefly discussed in the report.

2.0 GENERAL SCOPE

In general, variations in the atmospheric refraction index may be classified as:

- Small scale
- Large scale

Small scale variations are associated with clear air turbulence phenomena in the lower atmosphere and are manifested in random fluctuations of amplitude and phase of energy transferred through the medium, with time constants in the millisecond range. The large scale refraction index profile; of interest in this study, is a slowly varying property of an atmospheric path and a function of average values of local pressure, temperature and humidity along the path.

The refractive index, n, of the atmosphere is conveniently described in terms of the refractivity N, in parts per million by the expression:

$$n = 1 + 10^{-6} N \qquad (1)$$

The refractivity at optical wavelengths is related to local temperature and pressure by:

$$N \approx 77.6 \frac{P}{T} + 3.73 \times 10^5 \frac{e}{T^2} \qquad (2)$$

where: P = ambient pressure in millibars

T = temperature in degrees Kelvin

e = water vapor partial pressure in millibars

The downward bending curvature of a ray propagating at a given altitude level is given by the local gradient of refractivity:

$$C = -\frac{dN}{dh} = \frac{77.6}{T}\frac{\partial P}{\partial h} + \left[77.6\,\frac{P}{T^2} + 7.45 \times 10^5\,\frac{e}{T^3}\right]\frac{\partial T}{\partial h} + \frac{3.73 \times 10^5}{T^2}\frac{\partial e}{\partial h} \qquad (3)$$

The effect of humidity is appreciable for RF and microwave propagation. At optical frequencies however, the humidity effect is negligible and only temperature variations must be considered.

Absolute values of local temperature humidity and pressure as a function of altitude entering in equation (3), may be estimated within a small error from reported data for given geographic area and measured ground (or ocean) temperature. Similarly, close estimates on pressure gradients are obtained from universal curves. The situation however is quite different for the case of local temperature and humidity gradients. At the lower altitudes changes in the gradient direction (i.e., inversions) of temperature occur frequently as a result of many variables (e.g., position of the sun, overcast condition, surface and ambient temperature, wind velocity and direction). Likewise, frequent variations occur in the gradients of the humidity profile at the lower atmosphere.

Measured temperature gradients at lower altitudes using radiosonde techniques are shown in Figure 1. The double inversion in the gradient (superadiabatic) is typical for mid-day condition whereby the surface temperature is higher than the surrounding ambient temperature. The neutral gradient shown in Figure 1 is

FIGURE 1. RADIOSONDE

MEASURED TEMPERATURE PROFILES

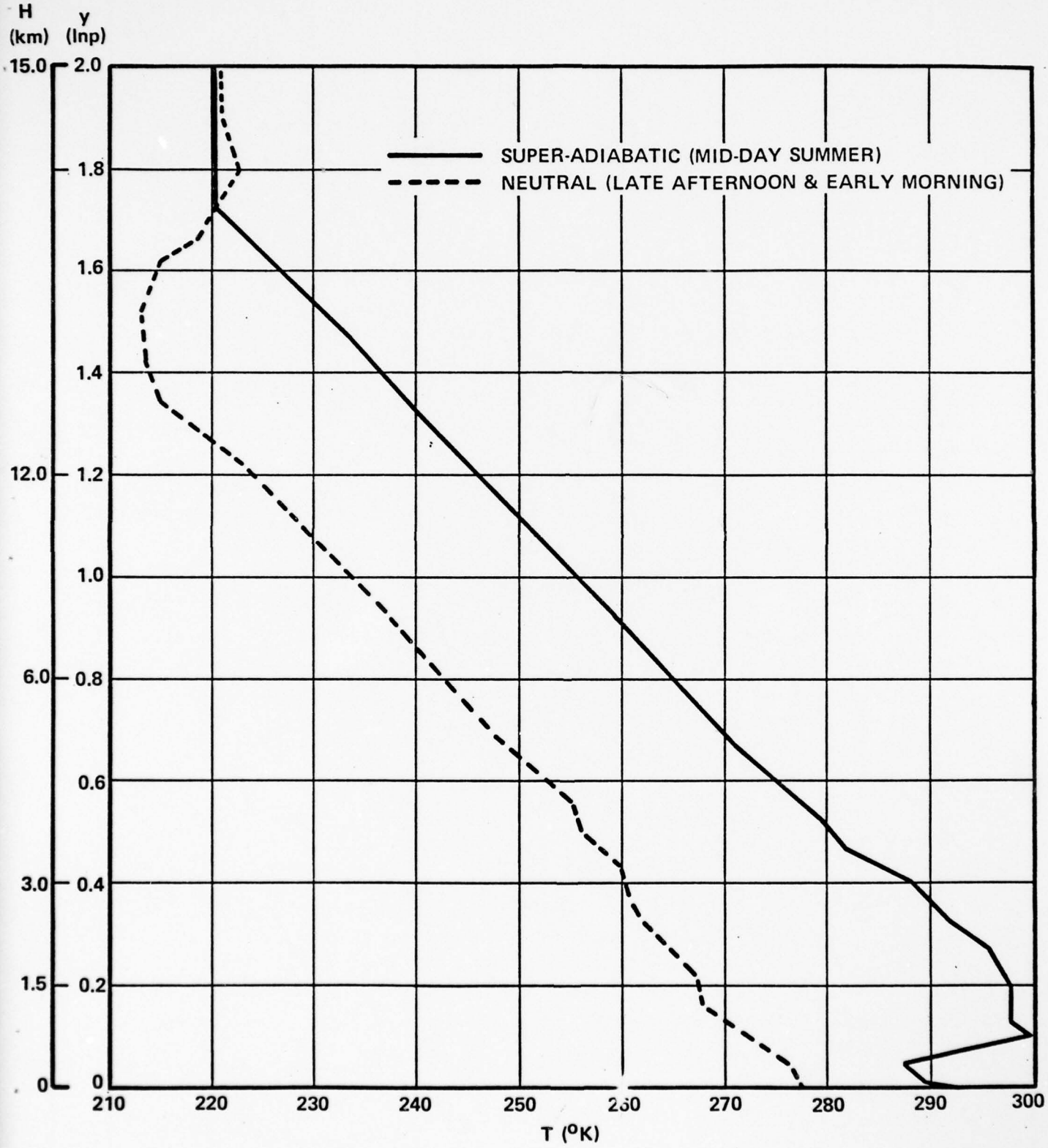

typical for early morning and later afternoon conditions. In addition a positive inversion at ground level may exist at night when the earth is cooling. It is clear that the uncertainty in the changing gradients of temperature in the vicinity of ground or ocean surfaces along with changing humidity gradients are the largest potential sources of error in estimating the line of sight refractive index.

The purpose of this study is to develop techniques for determining the fine structure temperature and humidity gradient profiles at the lower altitudes by means of high spectral resolution radiometric measurements. The profile information thus obtained should make it feasible to assess target error positions in real time systems.

3.0 BASIC PHENOMENOLOGY IN RADIOMETRIC PROFILING

The average apparent radiance sensed by a radiometer viewing the atmosphere is governed by the steady-state atmospheric radiation transfer equation as illustrated schematically in Figure 2.

For a downlooking radiometer (Figure 2A), the sensible radiance (neglecting scattering) is given by:

$$N_A = B_o(T)\ \tau_o + \int_o^{h_t} B_i(T)\ \frac{\partial \tau_i}{\partial h}\ dh \qquad (4)$$

where:

B_o, B_i = Planck's radiance at ground and i^{th} altitude level, respectively

τ_o, τ_i = atmospheric transmission coefficients in the total propagation path from ground level to receiver, and i^{th} altitude level to receiver, respectively

$\frac{\partial \tau_i}{\partial h}$ = kernel functions of the transfer equations

The first term in the right-hand side of equation (4) is due to the earth (or ocean) radiance as attenuated in its total propagation path. The second term represents re-emission of radiance in the various atmospheric layers within the propagation path.

The transfer equation for an up-looking radiometer (Figure 2B), is given by the integral:

$$N_A = \int_{\infty}^{h_o} B_i(T)\ \frac{\partial \tau_i}{\partial h}\ dh \qquad (5)$$

where the radiance is due to emission from the total atmosphere.

The method of fine structure profiling consists of implementing high spectral resolution sensor-channels, each selectively sensing emitted radiation from the constituent gas emission lines. As shown in Reference 3, the spatial resolution of a retrieved profile based on radiometric measurements is of the order of the spatial width of the kernel function in the spectral sensor channels.

An ideal up-looking radiometric system is depicted in Figure 3. As shown, it consists of a multitude of sensor channels, each having idealized rectangular narrow response characteristics, sensitive to radiation from discrete altitude levels. These idealized weighting functions would cause each channel to respond only to the radiation emitted in its respective altitude level, h_i. The actual channel responses however, are normally broadened by natural characteristics of the gaseous emission. Hence, the unique altitude behavior is not available and each channel indeed senses radiance from all altitudes. A crucial result of this effort therefore, is to obtain well behaved, peaked, weighting functions.

Basic parameters associated with radiometric profiling are defined in Figure 4, where a down-looking radiometer senses the radiation from an "atmospheric layer" within its field-of-view. The pertinent radiometric parameters are as shown:

$B_i(T)$ = Planck's radiance

$w_i(p)$ = partial pressure of active gas

$\epsilon(w,p)$ = gas emissivity

T = temperature

p = ambient pressure

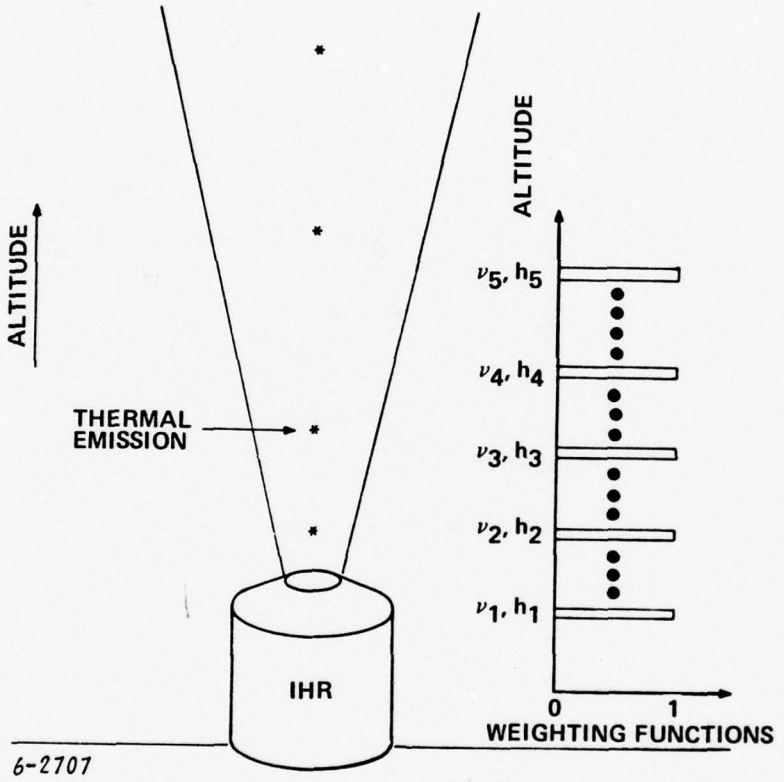

Figure 3. Ideal Profiling Radiometer Concept

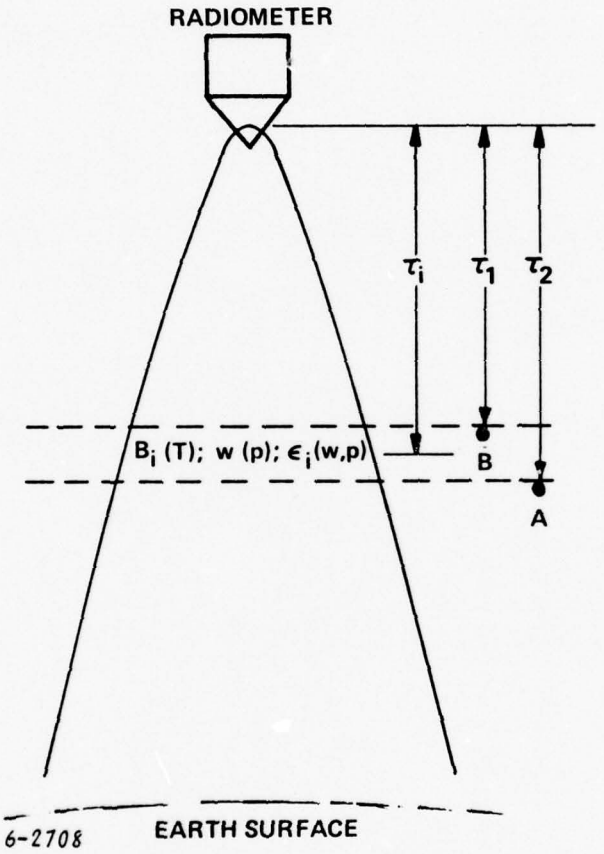

Figure 4. Sensible Radiance From Single Atmospheric Layer

It should be noted that though gas partial pressure and emissivity are also functions of temperature, this functional dependency is small as compared to that due to ambient pressure, and is neglected in the present discussion.

In the following discussion we examine the difference in shape characteristics associated with weighting functions for up-looking and down-looking radiometers.

The apparent radiance emanating from the i^{th} layer as sensed by the radiometer shown in Figure 4 is given by:

$$N_i = B_i(T) \quad \epsilon_i \tau_i \tag{6}$$

where τ_i is the transmission coefficient of the total path from i^{th} level to receiver.

To relate the apparent emission expression $\epsilon_i \tau_i$ to the weighting function expression we resort to Kirchoff's principle on emission-absorption equivalency. Referring to Figure 4, assume a radiance source $B_s(T)$ alternately located at points A and B; i.e., below and above the atmospheric layer respectively. The apparent absorption within the layer is then given by:

$$N_{ABS} = B_s(T) \quad \left[\tau_1 - \tau_2\right] \tag{7}$$

From Kirchoff's law of absorption-emission equivalency, the multiplying coefficients of Planck's radiance in equation (6) is equivalent to the transmissivity difference in equation (7), which may be expressed in a differential form, namely:

$$\Delta\tau_i = \tau_1 - \tau_2 = \frac{\partial \tau_i}{\partial h} \, dh \tag{8}$$

The spatial derivatives $\frac{\partial \tau_i}{\partial h}$, are the kernels of weighting functions and are linear coefficients of the temperature dependent Planck's radiance in equations (4) and (5). The spatial selectivity of a radiometer is thus determined from the response characteristics of the kernels as a function of altitude.

The difference in the nature of the kernel responses for up-looking and down-looking radiometers, sensing down and upwelling radiation respectively, may be visualized by referring to Figure 5. For a down-looking radiometer (Figure 5A), the concentration of the active gas and hence its emissivity is decreasing in consecutive atmospheric layers along the direction of radiation (as the observer moves closer to the radiometer). The transmission coefficient from each consecutive layer on the other hand, increases. Hence, peaking of the product $\epsilon\tau$ and its equivalent weighting function will occur somewhere along the propagation path. For an up-looking radiometer however, no peaking will occur since both the concentration and the transmission increase along the direction of radiation as shown in Figure 5B.

Typical altitude dependence of monochromatic weighting functions are shown in Figure 6 for a down-looking system, and Figure 7 for an up-looking system. As may be seen from the figures, unlike the down-looking case, no peaking in the kernel response result in up-looking radiometers. Hence, the spatial resolution of a direct sensing up-looking radiometer is inherently poor.

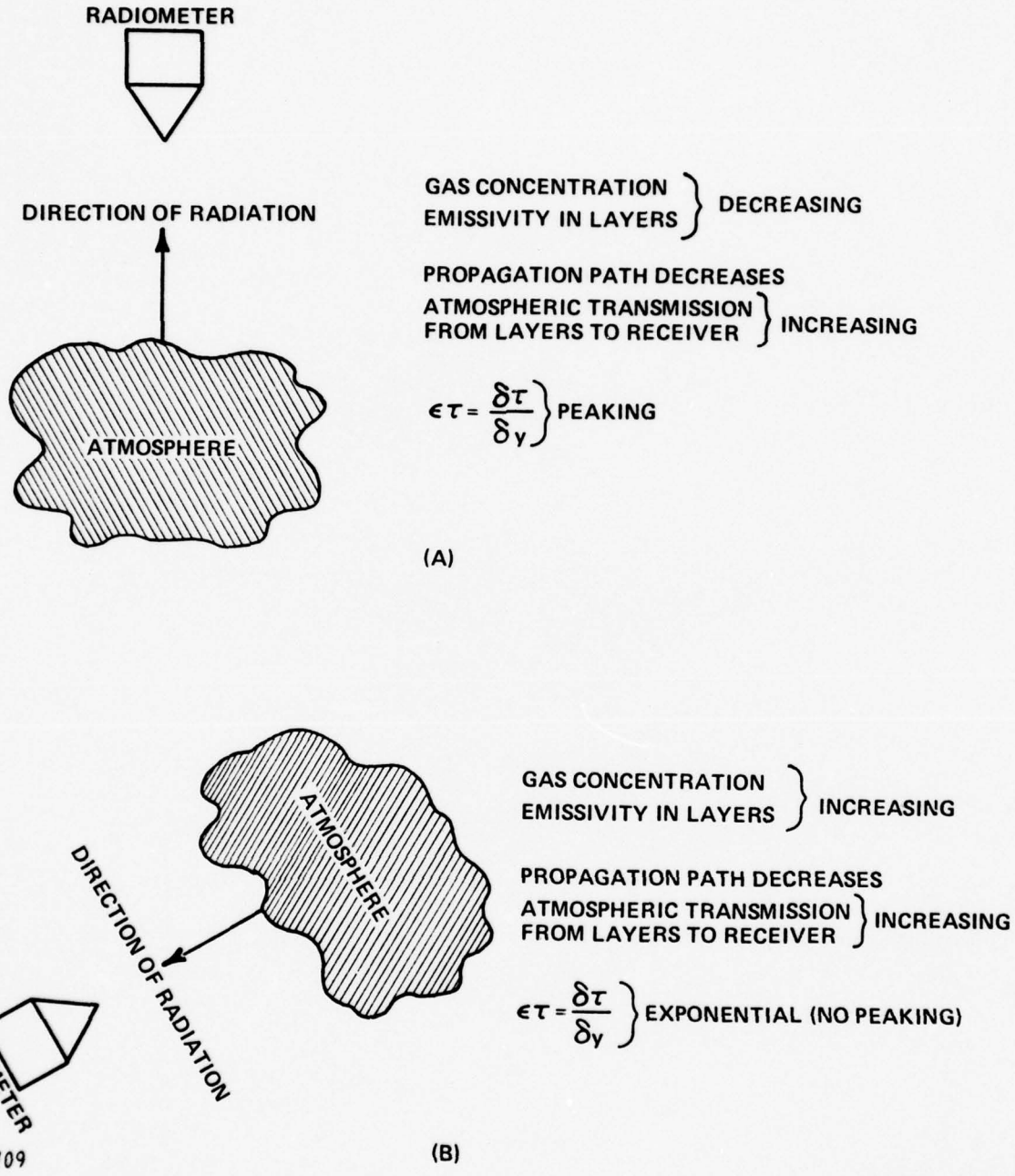

Figure 5. Behavior of Kernels for Up-looking and Down-looking Systems

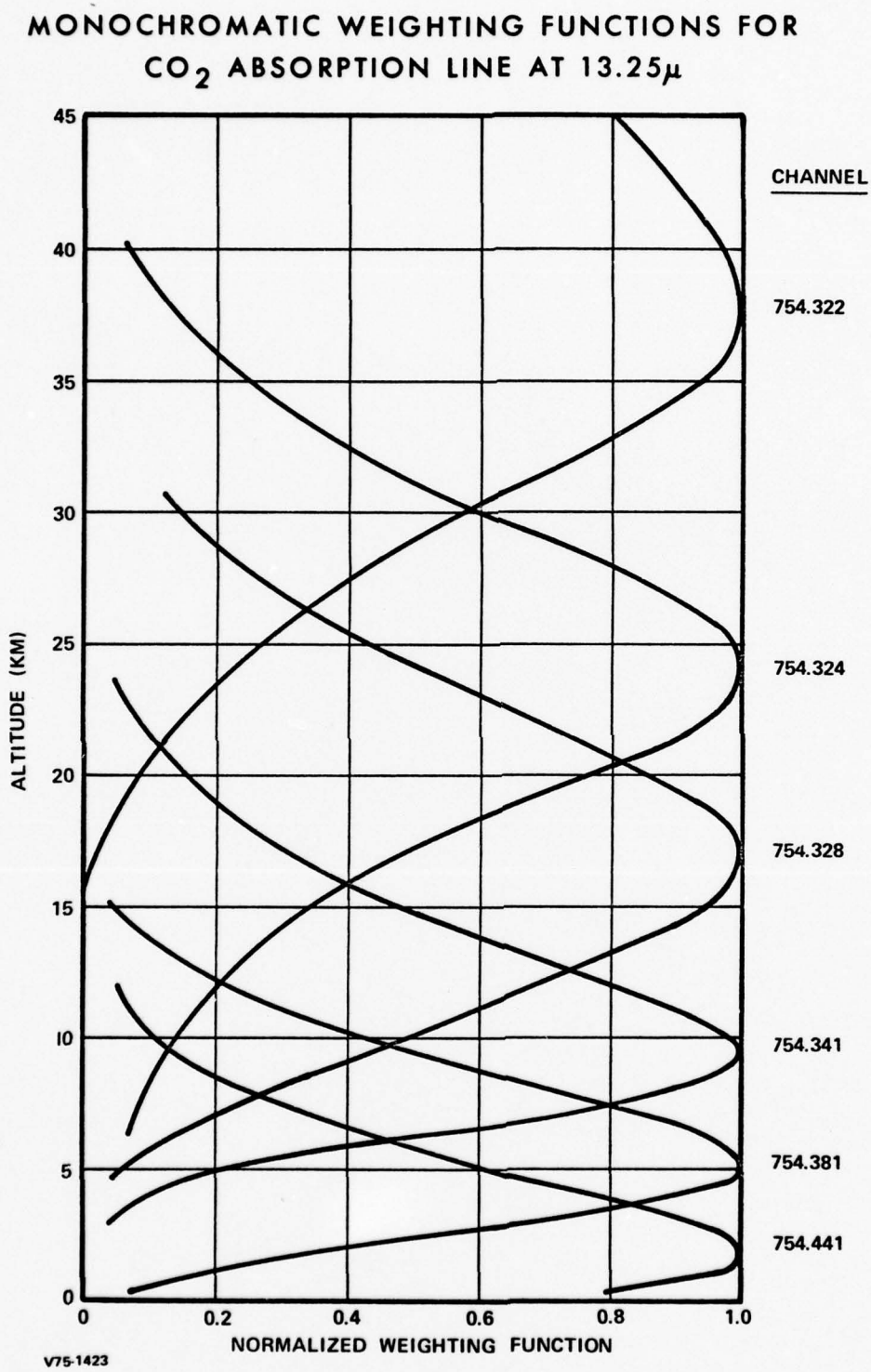

Figure 6. Typical Monochromatic Weighti .g Functions for a Down-Looking Radiometer

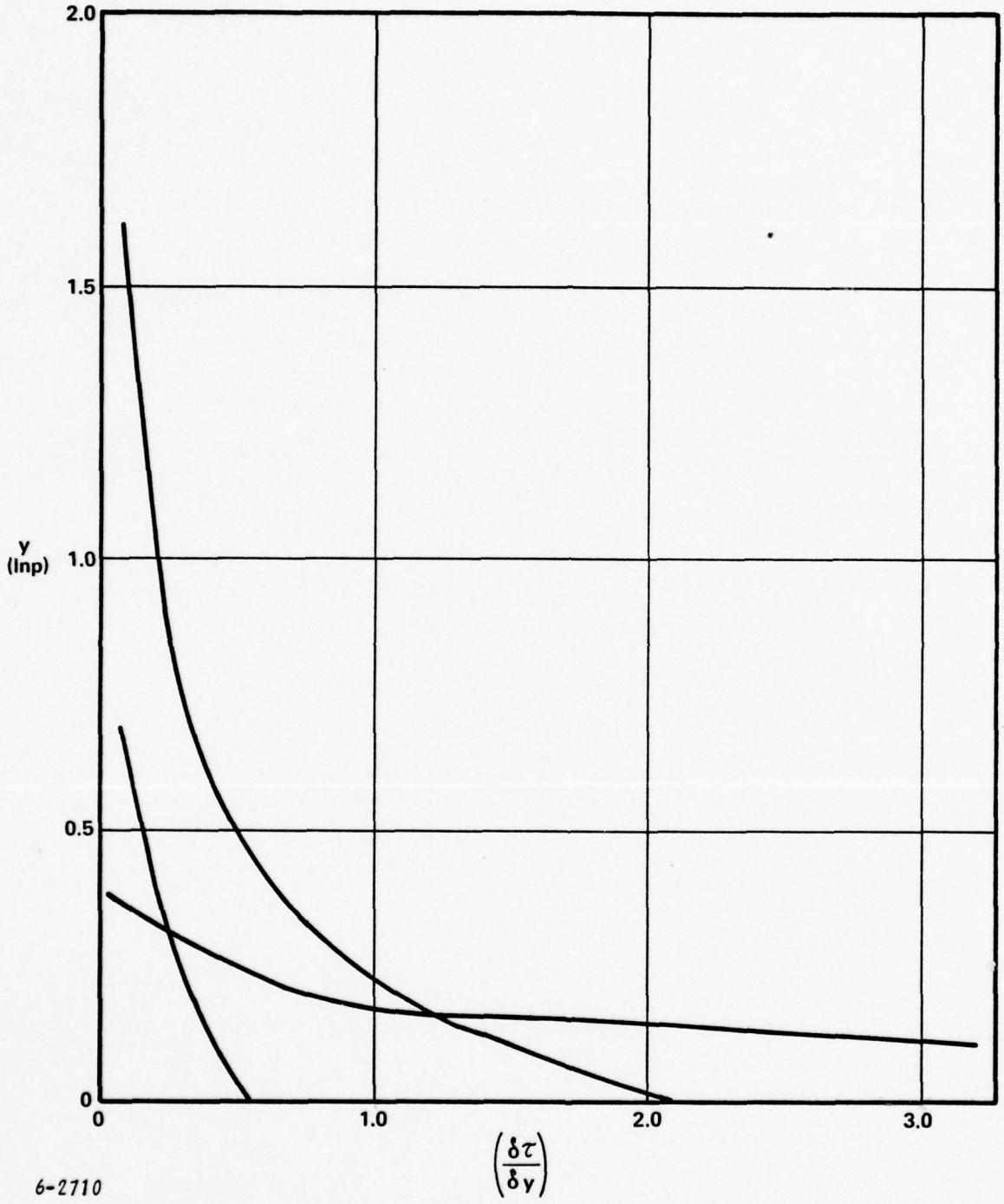

Figure 7. Typical Monochromatic Weighting Functions for an Up-Looking Radiometer

4.0 DIFFERENTIAL KERNEL APPROACH

From the above discussion it is clear that the weighting functions resulting in spectral channels of an up-looking radiometer based on direct sensing of downwelling radiation suffer from inherent poor spatial selectivity. This suggests that additional properties of the gaseous emission signature must be utilized in generating selective kernel functions for up-looking radiometers. The method developed on this program utilizes the steep spectral slope characteristics of single rotational line signatures. The technique requires sensing radiation from sections of single emission lines by means of high resolution spectro-radiometers. The information thus obtained enables the measurement of differences of radiances sensed from judiciously selected spectral positions with respect to the centers of line-pairs with predetermined signature strengths.

The basic mathematical relationships underlying the method of generating the spatially selective difference kernels are discussed in this section. The general expression of optical depth as a function of altitude is given in paragraph 4.1, and from it, mathematical expressions of kernel functions are derived in paragraphs 4.2 and 4.3. The general method for generating the spatially selective functions are discussed in paragraph 4.4. Plots of generated spatially selective difference kernels for carbon dioxide and water vapor are shown.

4.1 ALTITUDE FUNCTION OF A MONOCHROMATIC ATMOSPHERIC TRANSMISSION COEFFICIENT

Figure 8 illustrates a rotational transition line shape, with Lorentzian attenuation profile representing pressure regions in the near ground levels. The monochromatic absorption coefficient as a function of frequency is given by:

$$\alpha(\nu) = \frac{S}{\pi} \frac{\gamma}{(\nu-\nu_o)^2 + \gamma^2} \tag{9}$$

where: S = integrated line intensity

γ = half-width at half maximum intensity

ν, ν_o = variable and line center frequency (in wavenumbers), respectively

The altitude variation of the absorption coefficient is due to a linear dependency of linewidth with pressure:

$$\gamma = \gamma_o p \tag{10}$$

where:

$p = \frac{P}{P_o}$ = normalized pressure

P, P_o = pressure at altitude and ground levels, respectively

γ_o = linewidth at ground level

The total optical depth, $Q(H)$ from altitude H, to a ground based radiometer is a function of gas constituent distribution with altitude as well as variation of its absorption coefficient. Thus:

$$Q(H) = \int_0^H \alpha(h) \sec\theta \, w(h) \, dh = \frac{S \sec\theta}{\pi \gamma_o} \int_0^H \frac{p(h) \, w(h)}{C^2 + p^2(h)} \, dh \tag{11}$$

where:

$w(h)$ = gas content per unit path length as a function of altitude

$C = \frac{\nu-\nu_o}{\gamma_o}$ = frequency deviation from line center normalized to line half-width at STP

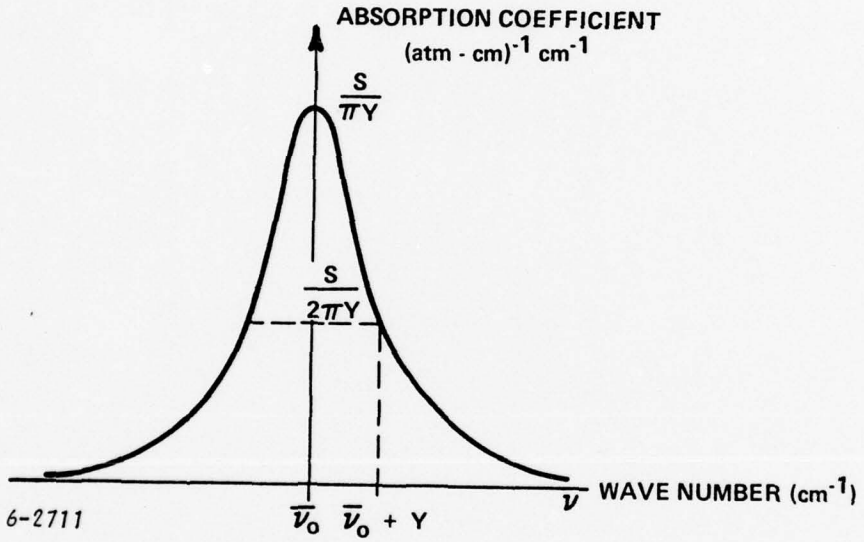

Figure 8. Lorentz Line Shape Profile

Θ = zenith angle of FOV

$p(h)$ = normalized pressure as a function of altitude

The transmission coefficient altitude dependency is given by:

$$\tau(H) = e^{-Q(H)} \tag{12}$$

4.2 MONOCHROMATIC WEIGHTING FUNCTION RELATIONSHIPS FOR UNIFORMLY MIXED GAS SIGNATURES

Signature bands of uniformly mixed gases, in particular the bands of carbon dioxide at infrared frequencies are utilized for temperature retrievals. The partial pressure of a uniformly mixed gas is linear with pressure, given by:

$$w(p) = w_o p \tag{13}$$

where: w_o = absorber content at STP in (atm-cm)/km. The variation of pressure with altitude is expressible by an exponential relationship:

$$p = e^{-y} = e^{-\frac{h}{h_o}} \tag{14}$$

where: h_o = scale height ($\approx$7.5 km)

y = scale height parameter

Substituting equation (13) into equation (11), and changing the variable of integration (from equation (14)); namely:

$$dp = \frac{1}{h_o} e^{-\frac{h}{h_o}} dh = -\frac{p}{h_o} dh \tag{15}$$

the optical depth of equation (11) is expressible as a function of local pressure, namely:

$$Q(p) = \int_1^p \beta \frac{p'}{C^2+p'^2} dp' = -\frac{1}{2} \beta \ln \left[\frac{C^2+p^2}{1+C^2}\right] \tag{16}$$

where:

$$\beta = \frac{S\ w_o}{\pi\ \gamma_o} \sec\theta$$

p' is a variable of integration

The transmission coefficient is now readily obtained by substituting the expression for optical depth (equation (16)) into equation (12):

$$\tau = \exp\left\{\ln\left[\frac{c^2+p^2}{1+c^2}\right]^{\beta/2}\right\} = \left[\frac{c^2+p^2}{1+c^2}\right]^{\beta/2} \qquad (17)$$

It is convenient to express the kernel as a spatial derivative with respect to the scale height parameter y; thus, from equations (17) and (14), the kernel function is given by:

$$\frac{\partial\tau}{\partial y} = \frac{\partial\tau}{\partial p}\ \frac{\partial p}{\partial y} = \frac{\beta}{(1+c^2)^{\beta/2}}\ p^2\ (c^2+p^2)^{\left(\frac{\beta}{2}-1\right)} \qquad (18)$$

4.3 MONOCHROMATIC WEIGHTING FUNCTION RELATIONSHIPS FOR WATER VAPOR SIGNATURE

Water vapor distribution in the atmosphere varies as a function of humidity conditions, and since its functional relationship with altitude is no longer linear, the transmission coefficient may not be expressed explicitly. The integral expression of the transmission coefficient as a function of the scale height parameter is generally given from equations (11), (12), and (14):

$$\exp\left(-\beta\int_o^{y_i} F(y)\,dy\right) \qquad (19)$$

where:

$$\beta = \frac{S\ h_o}{\pi\ \gamma_o}$$

$$F(y) = \frac{e^{-y}}{C^2 + e^{-2y}} w(y)$$

$w(y)$ = H_2O content per unit path length as a function of scale height parameter

The weighting function at altitude level y_i is then given by:

$$\frac{\partial \tau}{\partial y} = \beta F(y_i) \exp\left[-\beta \int_o^{y_i} F(y)\, dy\right] \qquad (20)$$

4.4 GENERATION OF DIFFERENCE KERNEL INFORMATION CHANNELS

A typical arrangement of channel positions for generating difference kernels is snown in Figure 9.

To first illustrate the existence of a peaked response in difference radiance kernels, assume one channel is tuned to line center with respect to line 1, and the other channel at the far wings with respect to line 2. Assuming a uniformly mixed gas, referring to equation (18), we have:

A. For the first channel:

$$C = 0 \qquad (21)$$

$$\frac{\partial \tau}{\partial y} = \beta_1 p^{\beta_1}$$

where β_1 = absorption coefficient of line 1

$$C \gg 1 > p \qquad (22)$$

$$\frac{\partial \tau}{\partial y} = \frac{\beta_2}{C_2^2} p^2$$

where β_2, C_2 are the absorption coefficient and normalized incremental frequency at line 2, respectively

The difference kernel Δ in the two channels is:

$$\Delta = \beta_1 p^{\beta_1} - \frac{\beta_2}{C^2} p^2 \qquad (23)$$

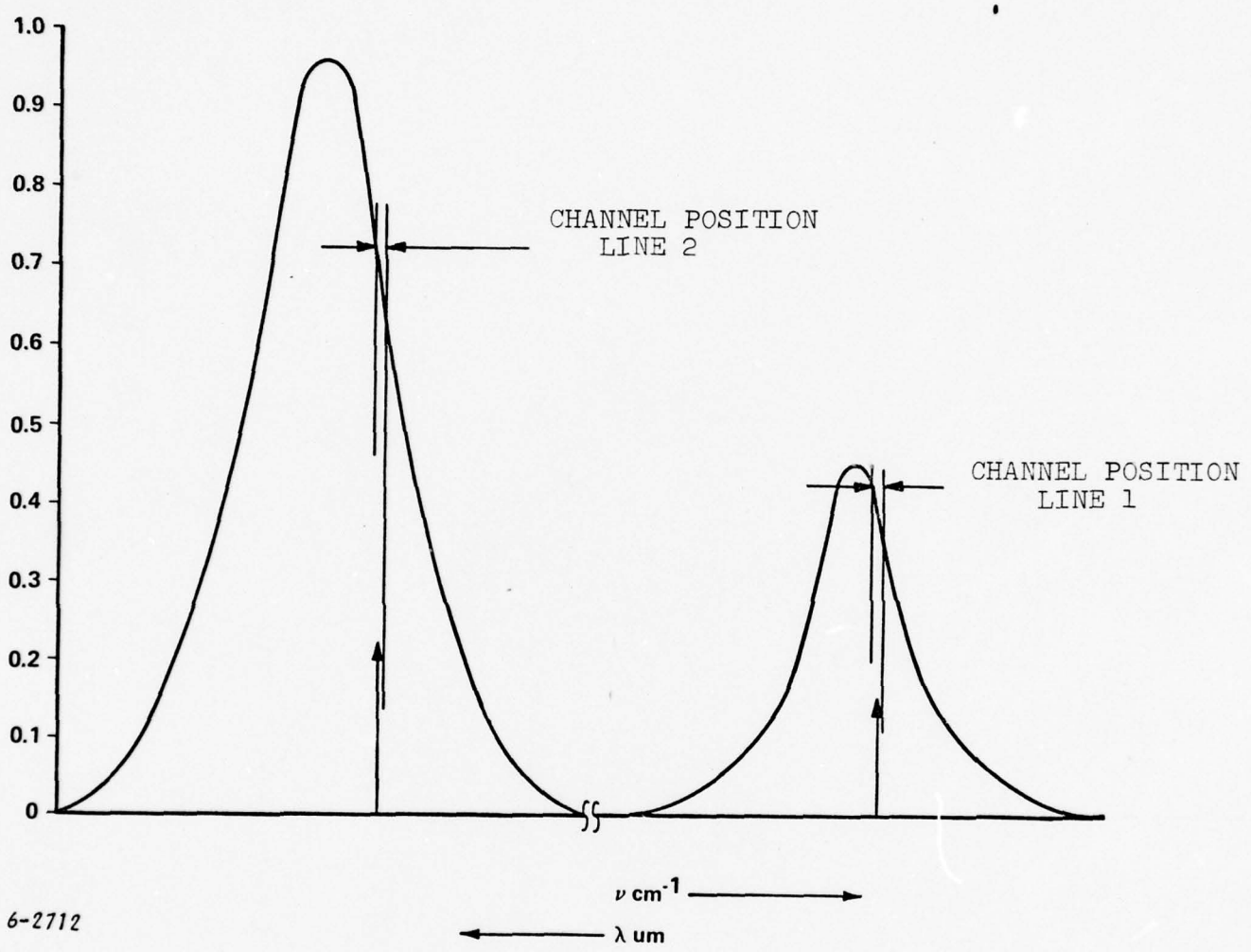

Figure 9. Schematic 2-Channel Arrangement for Generating Difference Kernels

The peak of the difference kernel is obtained by minimizing the function (23); namely:

$$\frac{\partial \Delta}{\partial y} = p^2 \left\{ \beta_1^2 \, p^{(\beta_1 - 2)} - \frac{2 \beta_2}{C_2^2} \right\} = 0 \qquad (24)$$

A minimum of the Δ-functions occur at infinity ($p = 0$), and a peak occurs at a pressure level:

$$P_{peak} = \left[\frac{2 \beta_2}{\beta_1^2 C_2^2} \right]^{1/(\beta_1 - 2)} \qquad (25)$$

Thus a peaked difference kernel results for the prescribed ratios of absorption coefficients and channel positions in the two lines. It should be pointed out however, that the difference kernel obtained from channels at extreme spectral positions are rather broad due to the shallow gradient at the far wing of the line. More selective difference kernels result for a channel position at a spectral region of steep slope in the absorption coefficient where the sensitivity to pressure variation is maximum.

The CO_2 emission band at 13 μm was considered for generating differential kernel functions for temperature profile retrieval. The technique however can be adapted to other spectral bands at infrared or millimeter wavelengths where discrete signature spectra due to uniformly mixed atmospheric gases exist.

The difference in kernels for two channels associated with two discrete lines, is given from equation (17) by:

$$\Delta = \left(\frac{\partial \tau}{\partial y}\right)_1 - \left(\frac{\partial \tau}{\partial y}\right)_2 = \beta_1 \left[\frac{C_1^2+p^2}{1+C_1^2}\right]^{\beta_1/2} \cdot \frac{p^2}{C_1^2+p^2} \qquad (26)$$

$$-\beta_2 \left[\frac{C_2^2+p^2}{1+C_2^2}\right]^{\beta_2/2} \cdot \frac{p^2}{C_2^2+p^2}$$

where: β_1, β_2 relate to signature strength of the two lines as defined in equation (14)

C_1, C_2 are normalized spectral positions of the two line channels

Line signature parameters and channel positions corresponding to weighting functions with peaks at prescribed altitude levels were found from solutions of minimized transcendental equations of the form:

$$\frac{\partial \Delta}{\partial y}\bigg|_{y = y_i} = 0 \qquad (27)$$

The computations were performed for various combinations of parameters so as to obtain optimum selective and contiguous difference kernel channels for altitude levels to about 5 km.

Figures 10 and 11 show difference-weighting functions obtained for vertical and 30-degree grazing-angle up-looking systems. As shown, narrower width difference kernels result at regions immediately above ground level and broadening toward higher altitudes. The dotted lines shown in the figures represent reversal in signs (foldovers) which will tend to degrade the retrieval accuracy. In general, appreciable negative response values in the vicinity of ground levels are undesirable. To that end the kernel functions

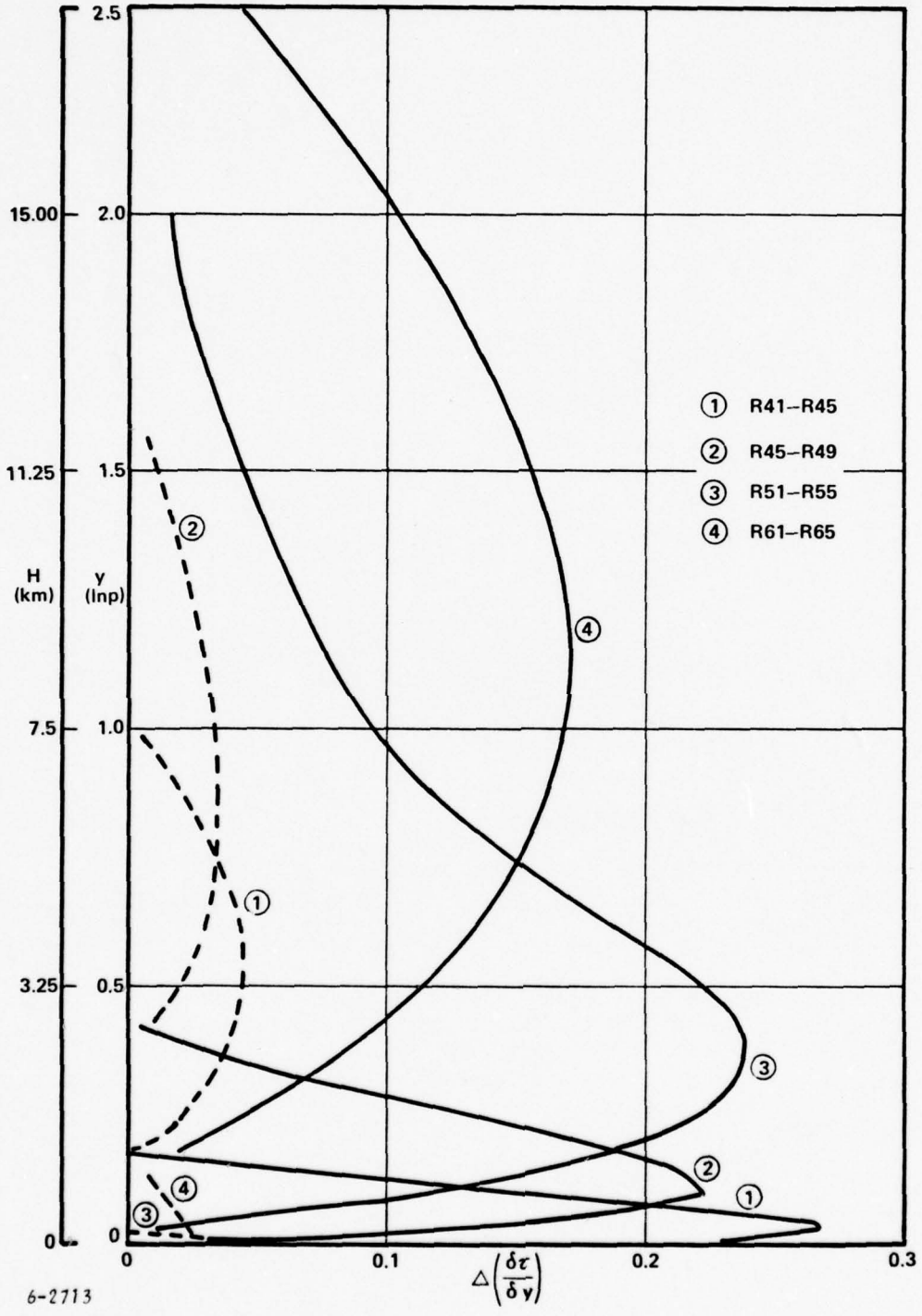

Figure 10. Differential Weighting Function of CO_2 Signature Emission For Vertical Up-Looking System

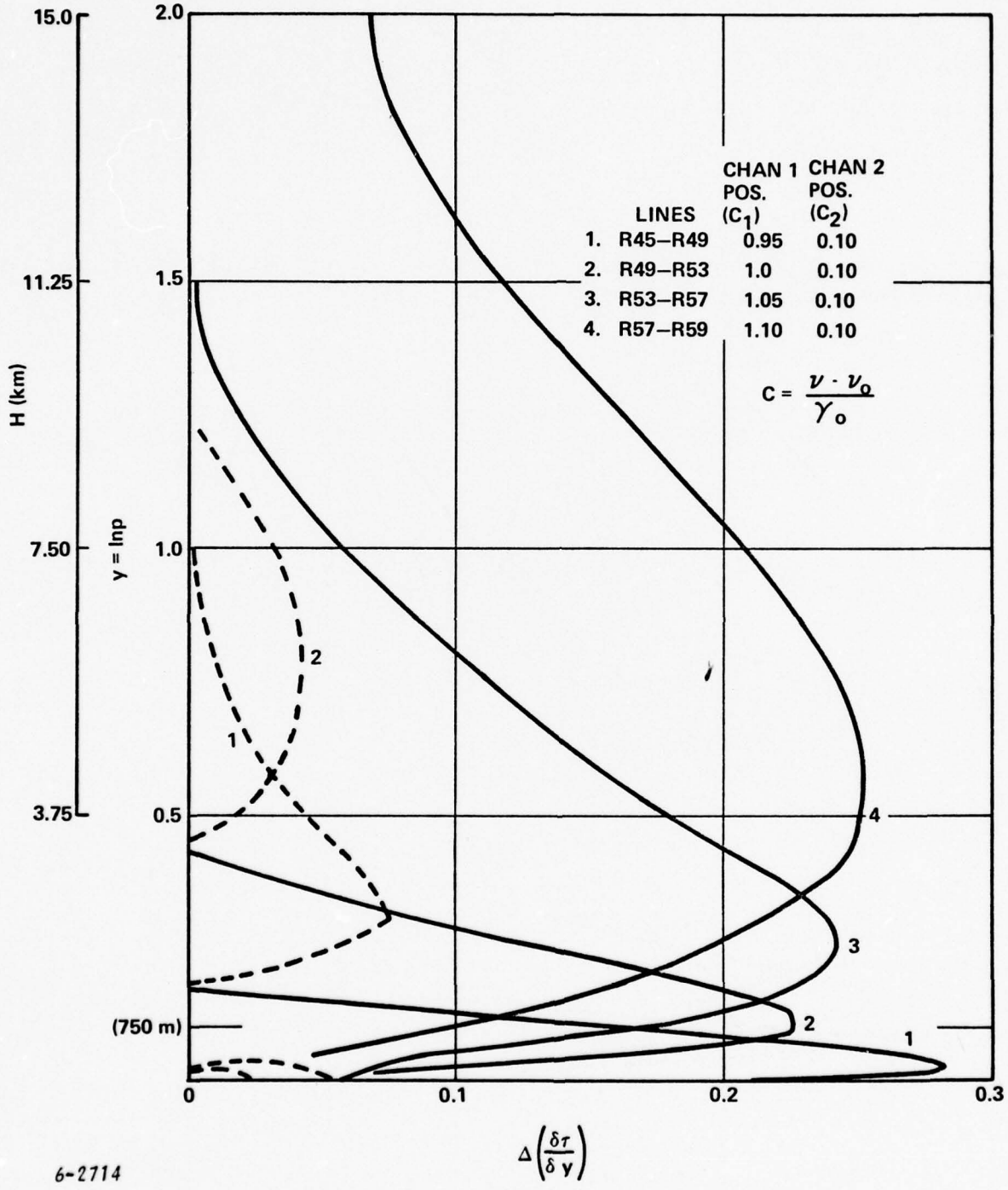

Figure 11. Differential Weighting Fu ctions for 30-Degree Grazing Angle Up-Looking System

should vanish at ground level which is accomplished by the proper selection of the relative spectral position C_1 and C_2 of the channels. Thus:

$$\Delta = 0 \qquad \text{at } p = 1$$

which results in a constraint on the absorption coefficient ratio given by:

$$\frac{\beta_1}{\beta_2} = \frac{1 + C_1^2}{1 + C_2^2} \tag{28}$$

Difference kernel functions were also generated for water vapor signature lines from the transmission integral equation (20), which are given by:

$$\Delta = \left.\frac{\partial \tau}{\partial y}\right|_1 - \left.\frac{\partial \tau}{\partial y}\right|_2 = \beta_1 F_1(y_i) \exp\left[-\beta_1 \int_o^{y_i} F_1(y)dy\right] - \beta_2 F_2(y_i) \exp\left[-\beta_2 \int_o^{y_i} F_2(y)dy\right] \tag{29}$$

Typical humidity distributions for standard atmospheres were assumed (Reference 4), and corresponding optical depths and channel positions were computed by using the 6-point Gaussian integration method on a computer.

Figure 12 shows contiguous peaked difference-weighting functions obtained for a 30-degree grazing-angle up-looking radiometer, for H_2O signature lines in the vicinity of 4.7 μm.

Results of computed simulated temperature retrievals using the present technique are discussed below in Section 5.

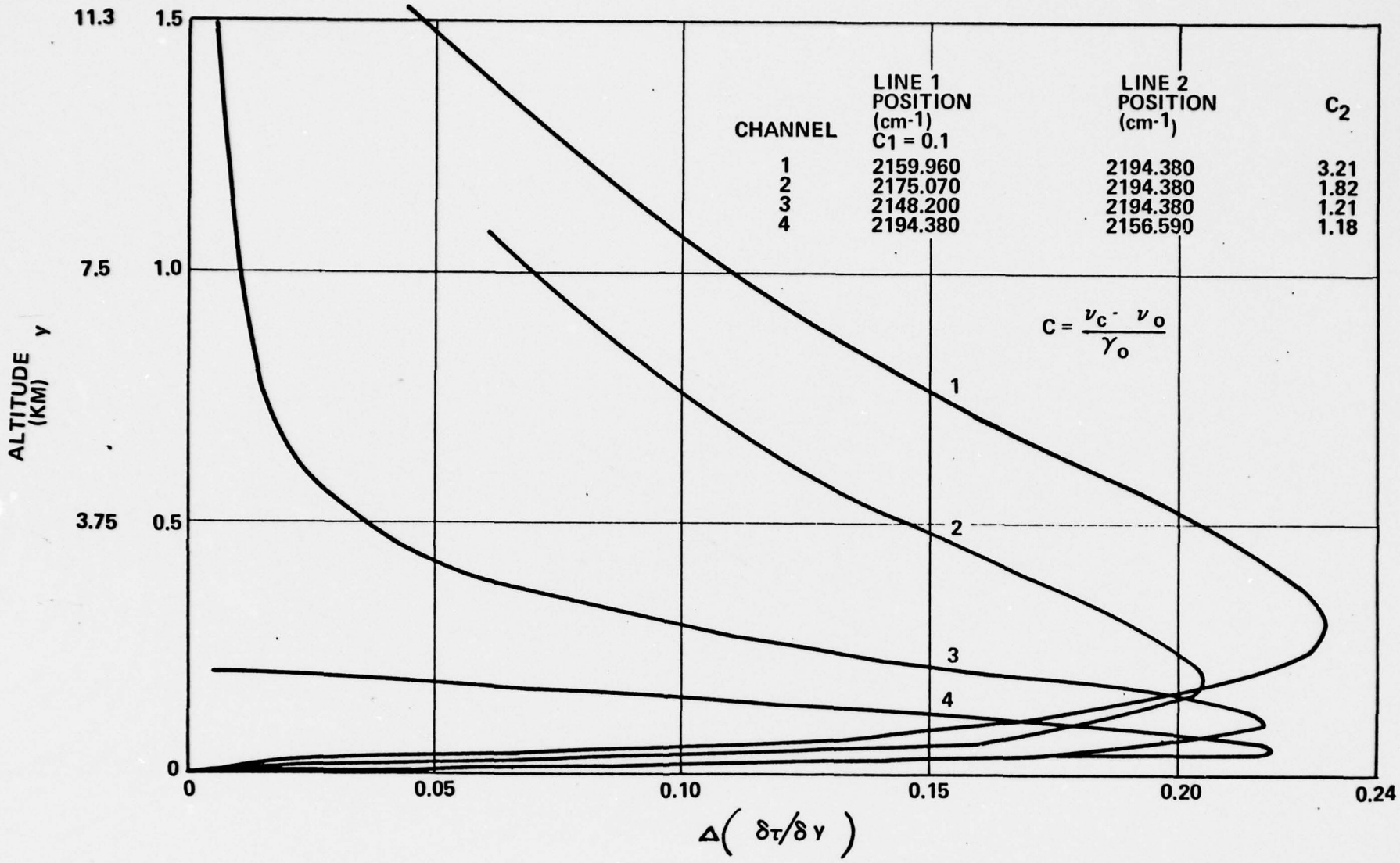

Figure 12.

DIFFERENTIAL KERNEL FUNCTIONS FOR WATER VAPOR ALTITUDE PROFILE RETRIEVAL

5.0 SIMULATED TEMPERATURE PROFILE RETRIEVALS

Retrievals of a typical superadiabatic lapse temperature profile were simulated on a computer using three and four difference-kernel information channels. The basic method and results obtained are discussed in the following paragraphs.

5.1 RETRIEVAL METHOD

The retrieval algorithm adapted is based on a modified inverse solution of the radiative transfer equation in conjunction with a relaxation iterative method of convergence (References 5 and 6). The advantage of this method over the inverse matrix retrieval techniques is that:

a) No apriori statistical knowledge on atmospheric parameters are required. The method is particularly suited for real time continuous profile updating systems at all geographic locations.

b) The resultant profile is generated from numerous solutions at small incremental and contiguous altitude layers.

The basic computer routines for a temperature simulated retrieval analysis, using the iterative method, are shown in the block diagram of Figure 13. A somewhat similar computational method may be adapted for humidity retrieval.

Referring to Figure 13, the basic computational steps are as follows:

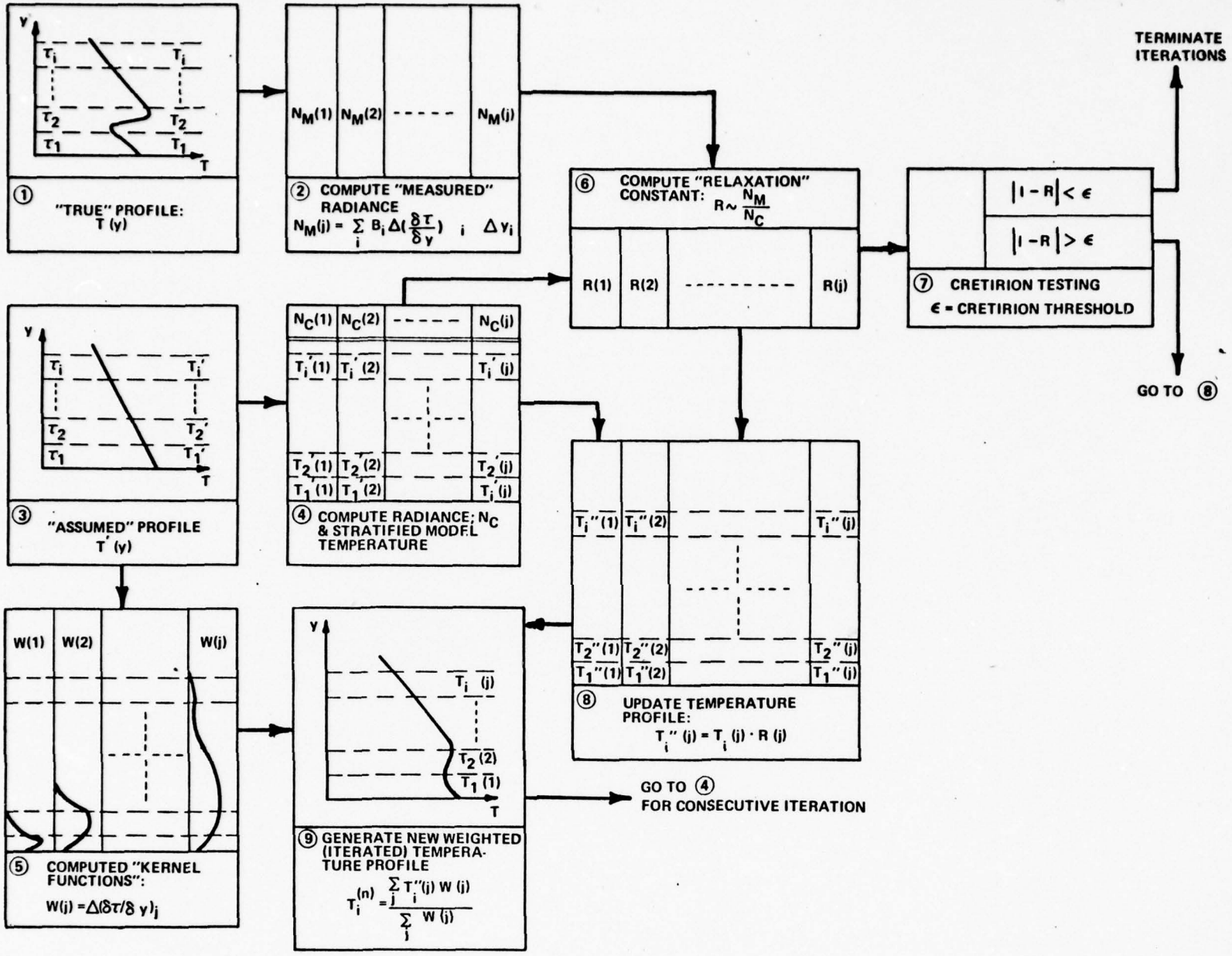

Figure 13.

BLOCK DIAGRAM OF COMPUTER SIMULATED PROFILE RETRIVAL

STEP 1.--A temperature altitude profile is first assumed, and designated as the "true" model atmosphere.

STEP 2.--The radiance differences at each signature channel corresponding to the "true" profile are computed from a digitized atmospheric model at discrete isobaric incremental regions, and are designated as "measured" values.

STEP 3.--An arbitrary temperature profile designated as a "guessed" model is then assumed, serving as a starting point in the iterative computational process. In consecutive iterations the model is updated by new generated profiles in Block 9.

STEP 4.--The "guessed" (or updated) profile is digitized at discrete isobaric layers, and difference radiances corresponding to the model in all signature channels are computed, and are designated as "computed" values.

STEP 5.--Difference kernel functions at each discrete spatial layer, and for each signature channel are computed based on the known concentration of the absorbing gas at the local pressure levels.

STEP 6.--A relaxation constant proportional to the ratio of "measured" to "computed" values is set for each signature channel. This constant is used for updating the model profile so as to converge to the "true" profile in a consecutive step.

STEP 7.--A criterion test is performed, based on the ratio value in step 6. If the ratio R in all signature channels is close to unity the iteration process is terminated. Otherwise, the process is continued at step 8.

STEP 8.--The discrete temperatures of the profile model (step 4) are updated in proportion to the relaxation constant corresponding to the given signature channel (step 6). In essence new updated temperature profiles are generated at each signature channel.

An iterated profile is finally obtained from the individual channel models (step 6), which is based on an average weighting in proportion to the kernel values corresponding to the channel at each altitude level.

The program has been written and executed for three and four difference kernel retrieval simulations. Tabulated spectroscopic signature parameters from Reference 7 were used. The profiles were retrieved in intervals of 37.5 meters for the first 750 meters and in 75 meter intervals from 750 to 2.25 km above ground level, and 750 meter intervals above 2.25 km. Between 30 to 50 iterations were required for convergence.

5.2 SIMULATED RETRIEVAL RESULTS

Simulated retrievals for an assumed superadiabatic temperature profile with a double inversion at 375 meters and 750 meters above ground level, were programmed on a computer.

Figure 14 shows a retrieval based on a three information channel system, with weighting functions as shown in Figure 11. Curve A in the figure is the assumed "true" atmospheric profile, curve B is the "arbitrary assumed" initial model in the iteration, and curve C is the retrieved model profile. As shown, the two

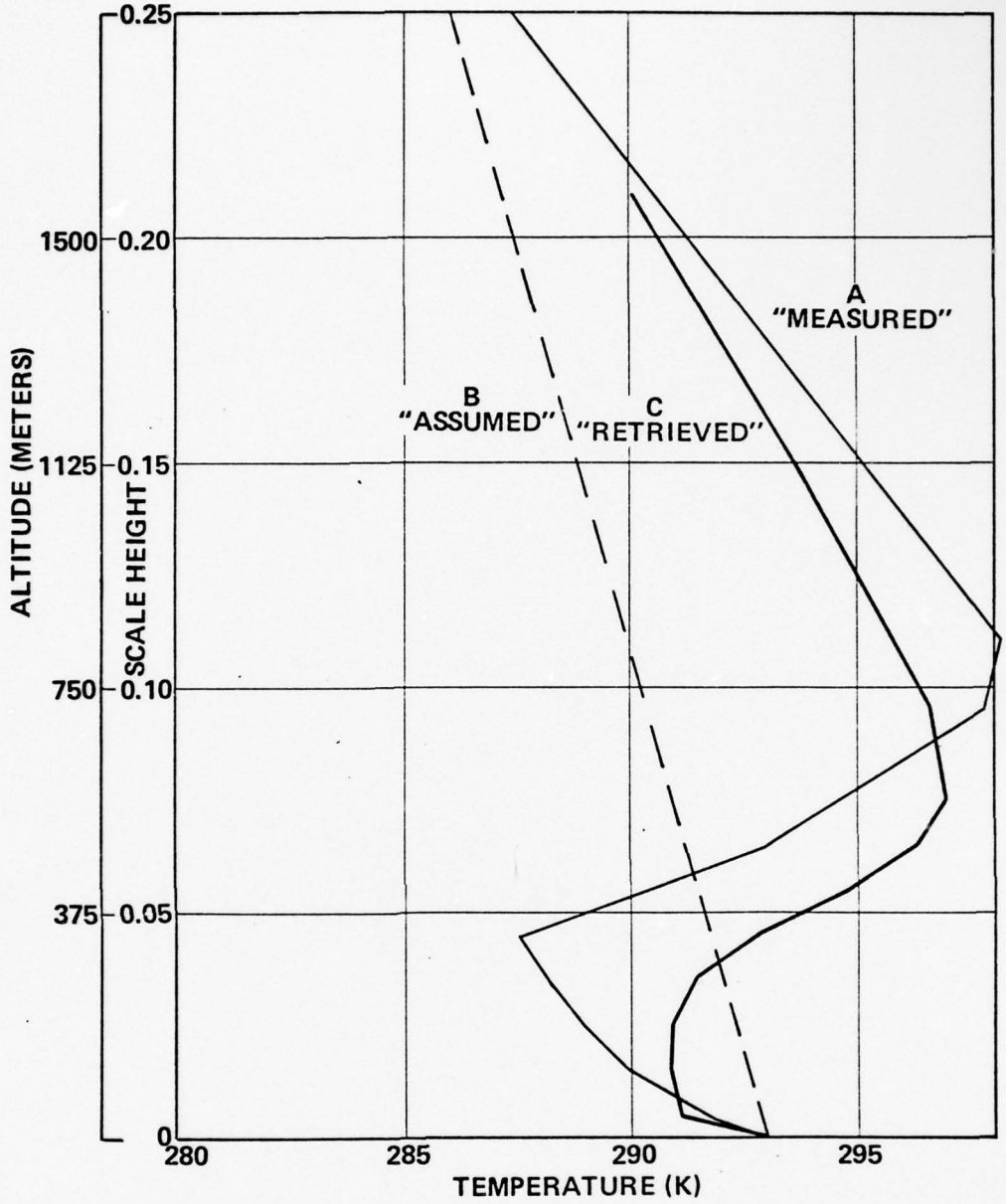

Figure 14. **COMPUTER SIMULATED RETRIEVAL (3 INFORMATION CHANNELS)**

inversions are reproduced in the retrieved profile with a displacement in gradient of 0.5 to 2°K on the temperature scale at the upper altitude levels and with a somewhat poorer fidelity immediately above ground level.

A retrieved profile obtained on the computer using four information channels with spatially narrower width weighting functions for channels in the vicinity of ground level, is shown in Figure 15. The fidelity of the profile gradient is considerably improved at the lower regions.

The discrepancies in the fine structure retrievals are the result of the negative foldovers in the difference kernels at upper altitudes. These introduce errors due to uncertainties in "measured" radiance differences associated with the information channels; an effect somewhat similar to that produced by system noise. Hence, no further degradations due to noise are expected to occur for systems having reasonable high signal-to-noise ratios.

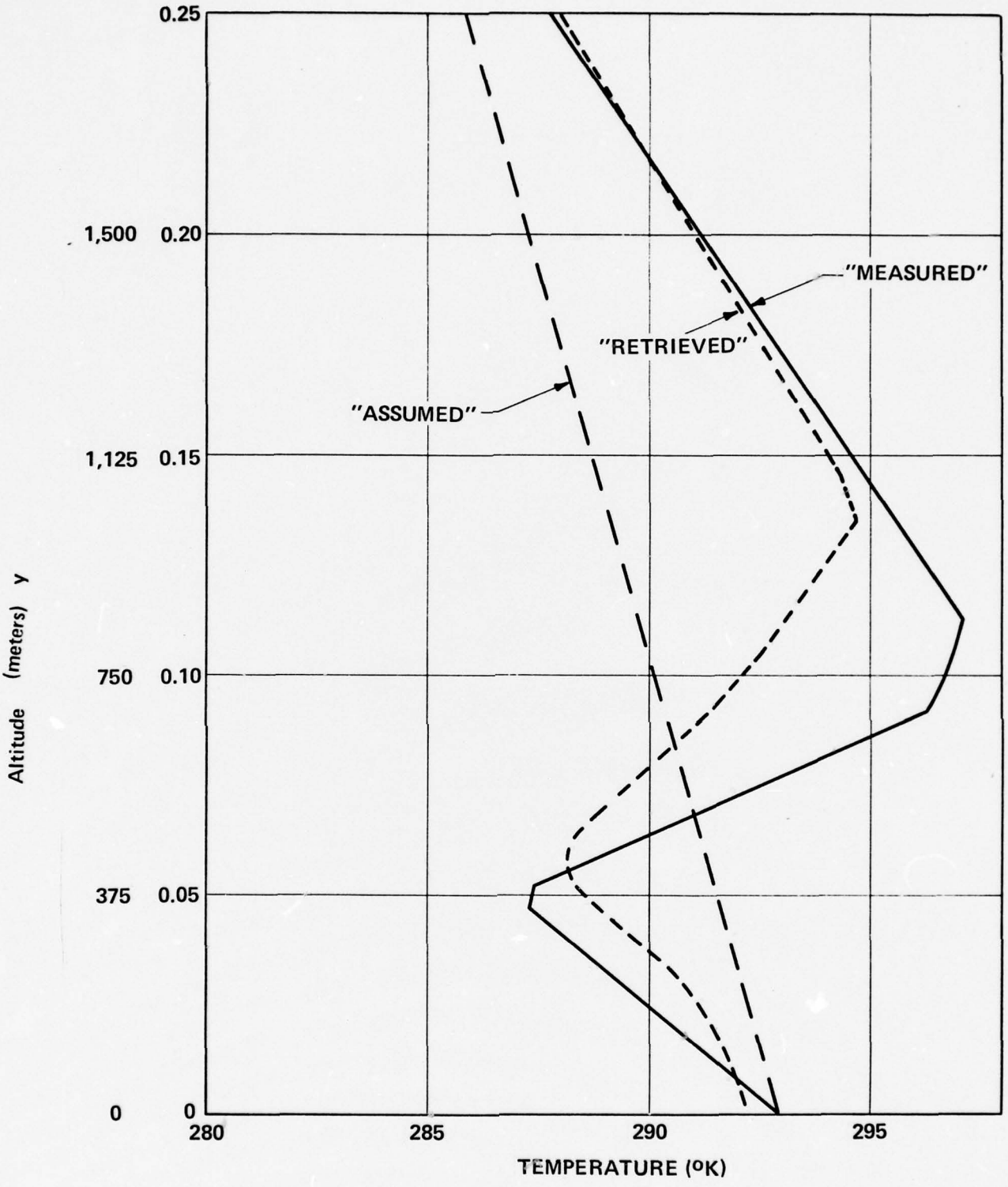

Figure 15 COMPUTER SIMULATED TEMPERATURE ALTITUDE PROFILE RETRIEVAL (4-CHANNEL SYSTEM)

6.0 SYSTEM SENSITIVITY CONSIDERATIONS

As discussed in Section 5, the present technique of selective profiling is based on quasi-monochromatic measurements of radiance differences at prescribed spectral positions with respect to absorption line pairs. Thus very high spectral resolution in the radiometric channels is required. Hence, there are two key requirements associated with the spectro-radiometric instrumentation, namely:

a) High spectral resolution. The instrument must be capable of resolving spectra of the order of 10^{-3} to 10^{-4} cm^{-1} (i.e., approximately 1 percent of absorption linewidth).

b) High sensitivity. The instrument must be capable of sensing small signal differences from narrow spectral width channels with sufficient signal-to-noise ratios.

Two candidate systems suitable for remote detection with the required high resolution were investigated on the program:

a) The coherent infrared heterodyne radiometer (IHR)

b) The Fabry-Perot Etalon (FPE) spectro-radiometer

In the IHR technique, a laser local oscillator signal (e.g., tunable diode laser), is coherently mixed with an incoming source irradiance, resulting in an intermediate frequency (IF) at the output of the photomixer. Extremely high spectral resolution is attainable with an IHR which ultimately is limited only by the stability of the laser source.

The FPE spectrometer basically consists of two high reflective parallel plate mirrors, whereby high resolution bandpass response characteristics result from interferences of multiply reflected beams. The spectral resolution in the FPE is ultimately limited by achievable etalon finesses and considerations of complexity in practical implementations of multi-etalon structures required for rejecting higher order passbands.

An analysis on relative merit and performance limits of the two spectral techniques for the present application is given below. Key spectral techniques associated with FPE are also discussed in this section.

6.1 IHR SENSITIVITY

The sensitivity of a properly designed IHR system is quantum-noise-limited at the operating optical frequency. The noise equivalent power (NEP), defined as the input signal required to result in a signal-to-noise (SNR) of unity, is hence given by:

$$NEP = hf\sqrt{\frac{\Delta f}{\tau}} \quad \text{(watts)} \tag{30}$$

where: f = optical frequency (Hz)

h = Planck's constant (watts-sec^2)

Δf = IF bandwidth (Hz)

τ = video integration time (sec)

For a spectral signal radiance (ΔN), resulting from a difference signal in an absorption line pair, the detected signal power is given by:

$$P_D = \frac{1}{2}\,\eta\, A_o\, \tau_o \Omega\, \Delta N\, \Delta\nu \tag{31}$$

where:

η = quantum efficiency

A_o = aperture area (cm^2)

τ_o = optical efficiency

Ω = solid angle field of view (sr)

ΔN = spectral radiance difference ($W/cm^2\text{-sr-}cm^{-1}$)

$\Delta\nu$ = optical bandwidth (cm^{-1})

and the factor $\frac{1}{2}$ accounts for polarization selection heterodyne rejection.

For optimum efficiency of the IHR, the throughput defined as the product $\Omega\ A_o$, is diffraction limited requiring:

$$\Omega\ A_o = \lambda^2 \tag{32}$$

where: λ = wavelength (cm)

From relationships in equations (30), (31), and (32), and noting that:

$$f = c\nu$$

$$\Delta f = c\ (\Delta\nu)$$

$$\lambda = \frac{1}{\nu}$$

where: c = speed of light (cm/sec)

an expression for the SNR in an IHR is given by:

$$SNR = \frac{P_D}{NEP} = \frac{\Delta N \cdot \eta \cdot \tau_o}{2\ hc^{3/2}\ \nu^3}\sqrt{\Delta\nu\ \tau} \tag{33}$$

We define a noise equivalent spectral radiance, ΔN_{NE}, which corresponds to unity SNR. Thus, from equation (33), setting SNR = 1 and solving for ΔN:

$$\Delta N_{NE} = \frac{2\ hc^{3/2}\ \nu^3}{\eta\ \tau_o \sqrt{\Delta\nu \cdot \tau}} \qquad (34)$$

6.2 FPE SPECTRO-RADIOMETER SENSITIVITY

The sensitivity of a background limited (BLIP) operated FPE receiver is limited by fluctuations of background photons incident within its field-of-view, and within its spectral acceptance window. The total background power collected by the FPE radiometer, viewing a background scene with spectral radiance N_B is given by:

$$P_B = \eta\ A_o\ \tau_o\ \Omega\ N_B\ \Delta\nu \qquad (35)$$

where:

η = quantum efficiency

A_o = area of optical telescope (cm^2)

τ_o = optical efficiency

Ω = solid angle field of view (sr)

N_B = background spectral radiance as a function of temperature and emissivity ($W/cm^2\text{-}sr\text{-}cm^{-1}$)

$\Delta\nu$ = optical bandwidth (cm^{-1})

The corresponding number of photons, Q, generated in the detector over the duration of an integration time, t, is given by:

$$Q = \frac{P_B t}{hc\nu}\ \text{(number of photons)} \qquad (36)$$

where: $hc\nu$ = energy per photon (W-sec)

The number of fluctuating noise photons, $\bar{q}$, is given from Poisson statistics by the square root of the number of background photons:

$$\bar{q} = \sqrt{Q} \qquad (37)$$

and the corresponding noise power integrated over time t is given by:

$$P_N = 2\, hc\nu\, \bar{q}/t \tag{38}$$

where the factor of 2 accounts for generation-recombination noise processes.

Combining equations (35) through (38), the noise power is given in equation (39):

$$P_N = \left\{4hc\nu\ N_B\ \Delta\nu\ \eta\ \tau_o \Omega A_o\ t^{-1}\right\}^{1/2} \text{ (watts)} \tag{39}$$

For a given spectral signal radiance ΔN, resulting from a difference signal in an absorption line pair, the detected signal power is given by:

$$P_S = \eta\ A_o\ \tau_o \Omega\ \Delta N\ \Delta\nu \tag{40}$$

Thus the SNR is given from the above equations (39) and (40):

$$SNR = \frac{P_S}{P_N} = \Delta N \left\{\frac{\eta\ A_o \tau_o \Omega \Delta\nu}{4hc\nu\ N_B}\right\}^{1/2} \tag{41}$$

The noise equivalent signal spectral radiance ΔN_{NE} is obtained by setting SNR = 1 and solving for ΔN in equation (41):

$$\Delta N_{NE} = \left\{\frac{4hc\nu\ N_B}{\eta\ A_o \tau_o \Omega \Delta\nu t}\right\}^{1/2} \text{ (watts)} \tag{42}$$

The throughput properties of the FPE will now be considered. Since Fabry-Perot etalons have limited fields-of-view at any one resonant condition, energy incident appreciably off the optical axis will propagate with difference resonance properties in the etalon. The limitation on FOV Θ, due to this shift is given by:

$$\Theta = 2\sqrt{\frac{\Delta\nu}{\nu}} \text{ (rad)} \tag{43}$$

Thus, energy incident outside the angular FOV Θ will not contribute to signal power. The solid angle Ω in equation (42) is thus constrained by Θ from equation (43), and since:

$$\Omega = \frac{\pi}{4} \Theta^2 \ (\text{sr}) \tag{44}$$

the dependency of ΔN_{NE} on optical bandwidth is given by:

$$\Delta N_{NE} = 4 \frac{\nu}{\Delta\nu} \left\{ \frac{hc \ N_B}{\pi \ \eta \ \tau_o \ t} \right\} \ (W/cm^2\text{-sr-cm}^{-1}) \tag{45}$$

6.3 COMPARISON OF SENSITIVITY LIMITS IN AN IHR AND FPE SPECTRO-RADIOMETER

A comparison of ultimate sensitivities achievable in the two spectro-radiometric systems is shown in Figure 16. The values plotted are based on equations (34) and (45) for the IHR and FPE respectively and are normalized to a radiance of 300°K blackbody, thus representing the minimum detectable fractional change in an arbitrarily assumed ambient background with unity emissivity.

As may be seen from Figure 16, appreciably greater sensitivity results with a FPE radiometer as compared to the IHR, which is particularly pronounced at the shorter wavelengths where the IHR sensitivity is inherently lower. The inferior performance of the IHR results primarily due to the small throughput associated with a coherent receiver which requires a diffraction limited FOV. As may be noted, the minimum detectable spectral radiance values plotted in the figure are normalized to the square root of the optical bandwidth. Since the throughput in an FPE radiometer is a function of optical bandwidth, several parametric curves are shown in the figure.

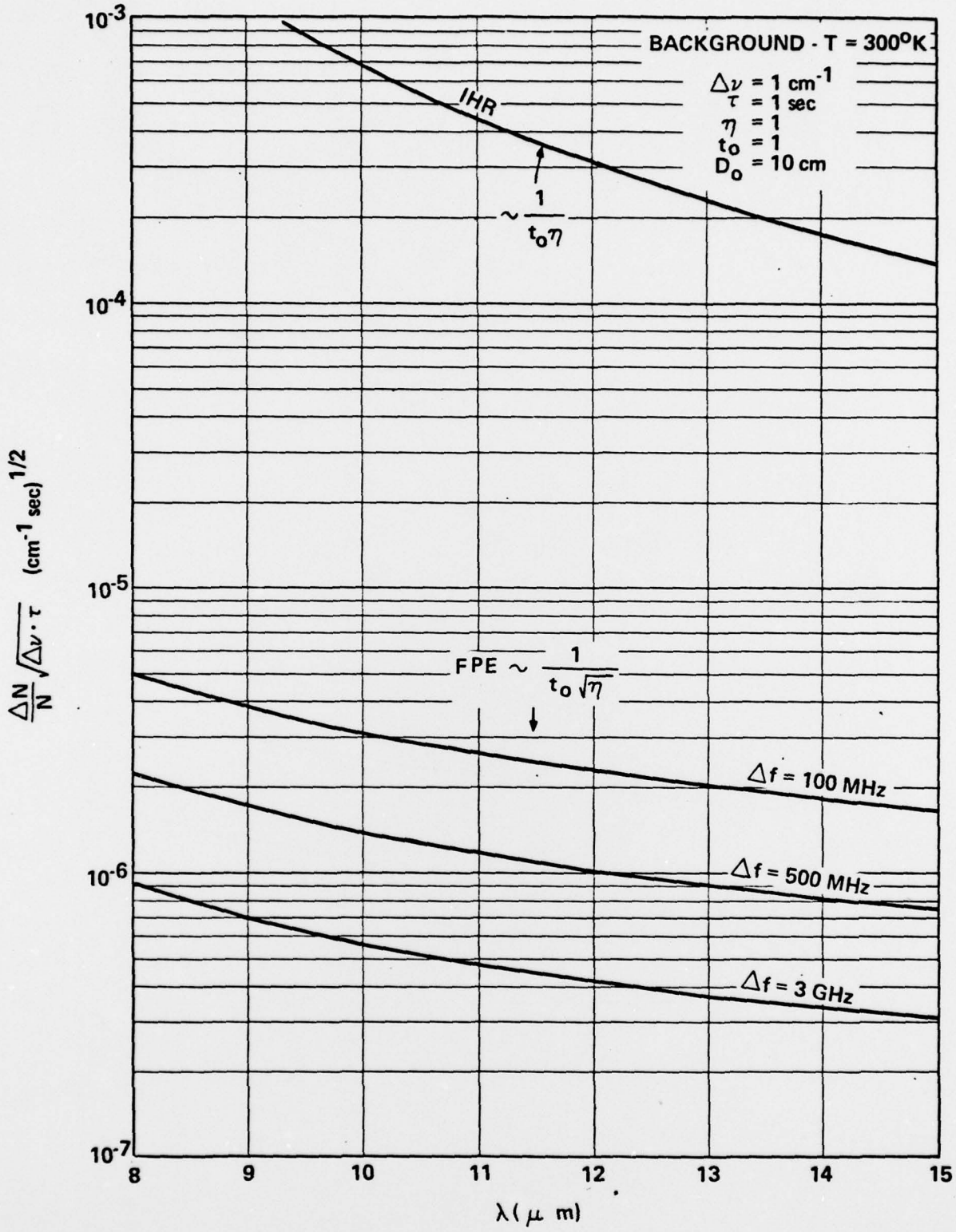

FIGURE 16. COMPARATIVE SENSITIVITY OF SPECTRO-RADIOMETIC SYSTEMS

6.4 ESTIMATED PERFORMANCE

An estimated sensitivity level of performance of an FPE spectro-radiometer implemented for temperature profiling is shown in Figure 17. The assumes system parameters are:

Diameter of optical telescope = 4"

Optical bandwidth = 3×10^{-4} cm^{-1} (100 MHz)

Quantum/optical efficiency = 30 percent

Observation time per measurement = 5 seconds

The bottom curve in Figure 17 represents the minimum resolvable fractional change in ambient (assumed here: T = 300°K, $\epsilon = 1$), corresponding to SNR = 1. The shaded area represents the range in the difference signal radiances resulting from pairs of absorption lines corresponding to various spatial selectivity channels. As may be seen, reasonably high SNRs are obtainable with the system.

Figure 18 shows required D* as a function of operating wavelength and the corresponding number of photon flux densities. Shown detectivity levels are within the state of the art of currently available detectors.

6.5 BASIC FPE SPECTROSCOPIC INSTRUMENTATION

A typical response of an FPE is shown in Figure 19. As shown, it consists of a multiplicity of periodic responses, each designated by an order m_i. The frequency spacing between two consecutive band passes, referred to as the free spectral range (ν_{FSR}), is a function of the optical path length between the two plates as shown in the equation in the figure. The ratio of the bandwidths to the free spectral range is given by the etalon finesse $\mathcal{F}$, which for ideal etalons is a function of plate reflectivity, however in practice is often limited by the achievable plate parallelism.

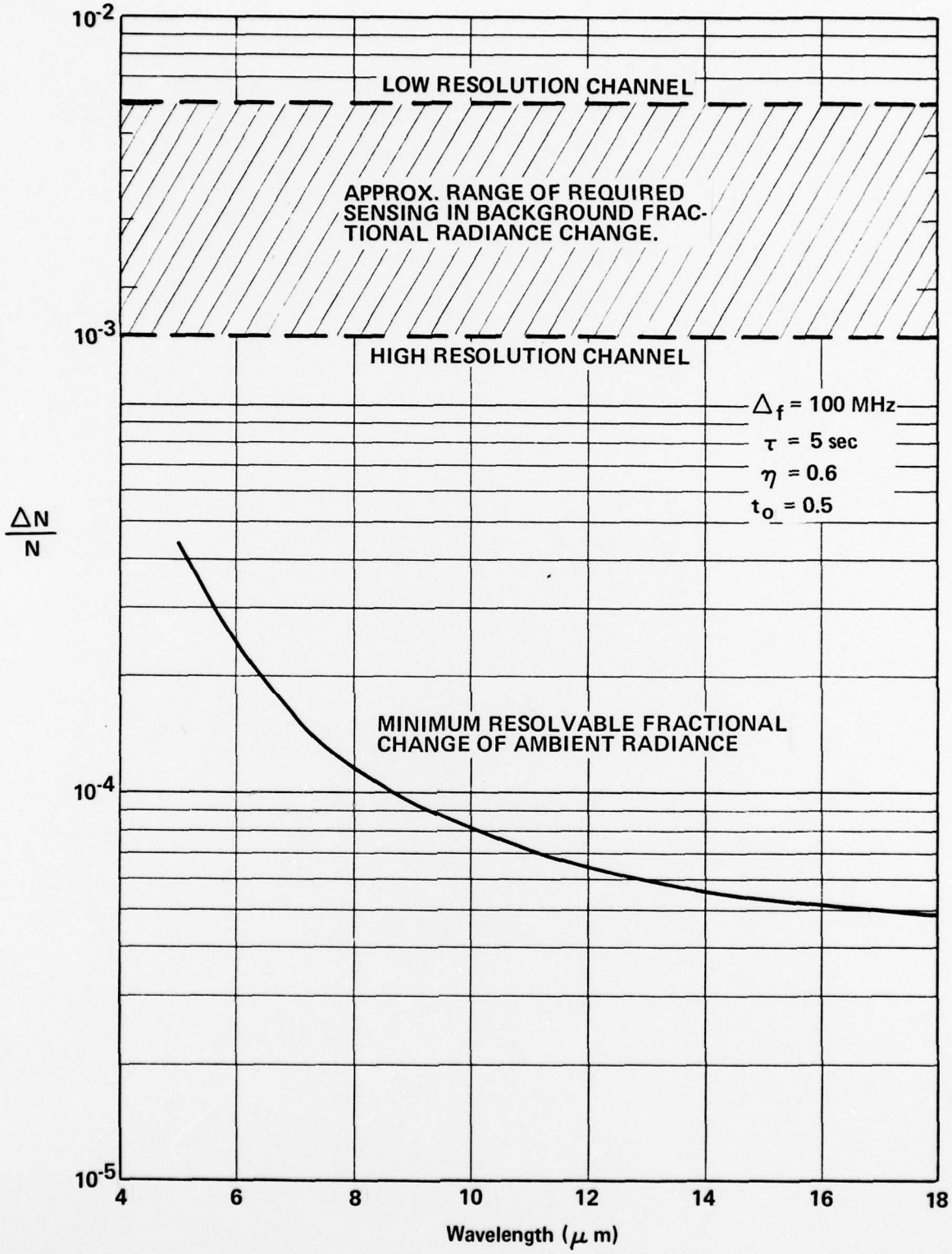

FIGURE 17. Performance Estimates of the FPE Spectro-Radiometer

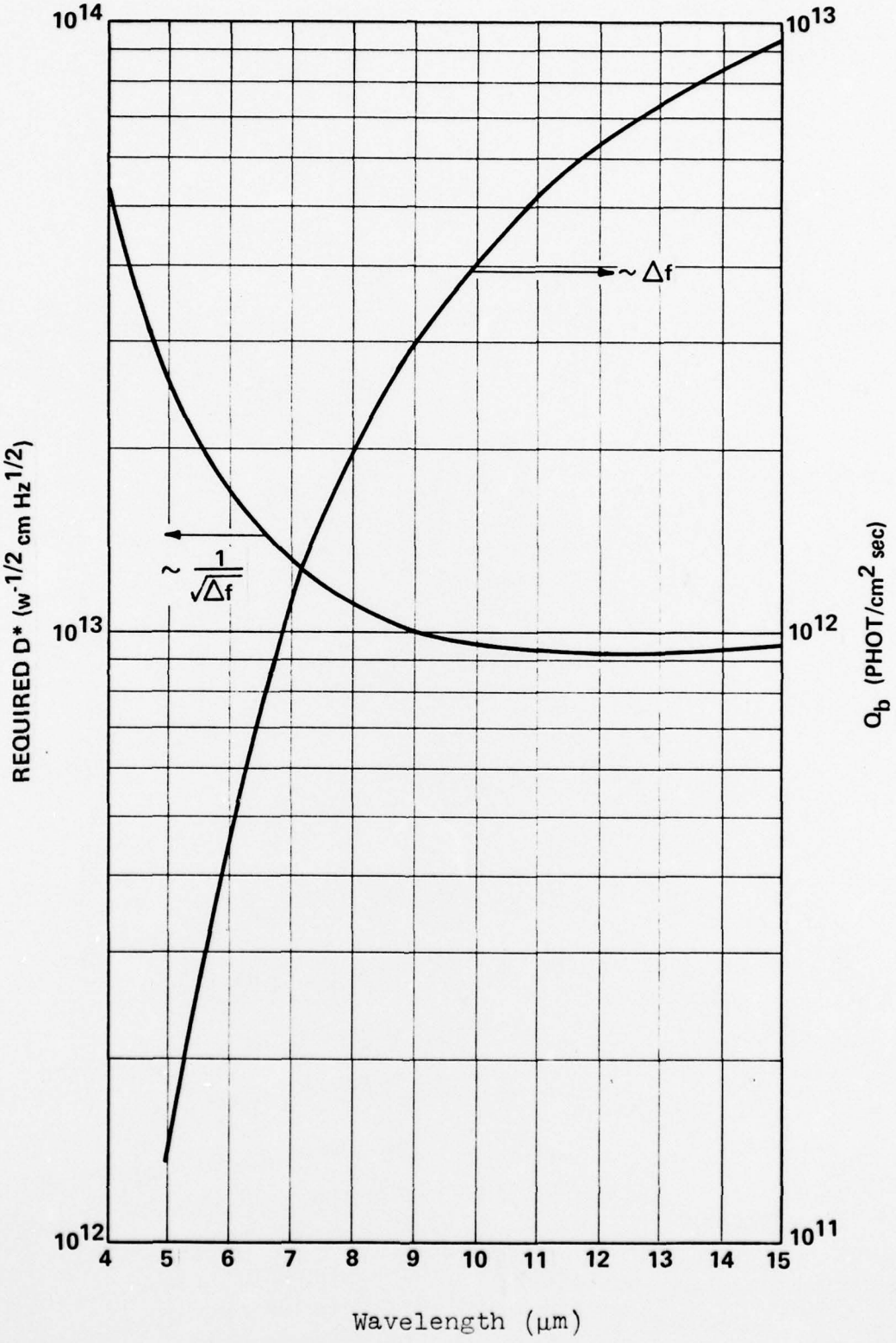

FIGURE 18. **REQUIRED RECEIVER SENSITIVITY**

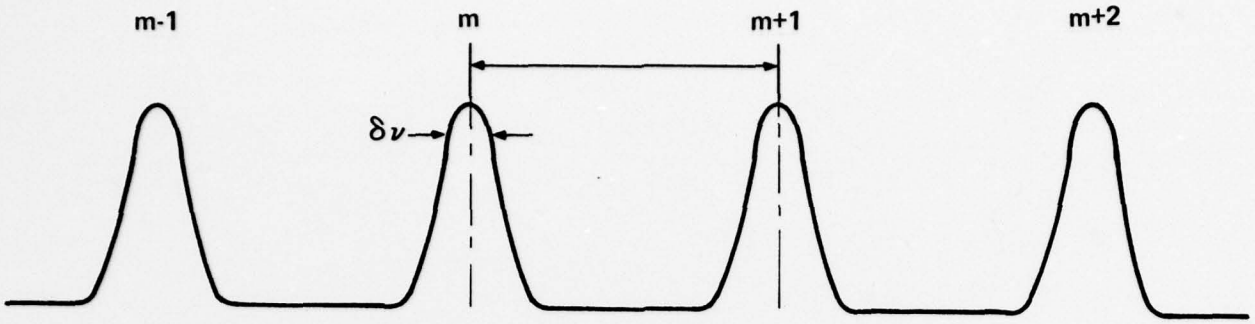

$$\delta\nu = \frac{\nu_{FSR}}{F}$$

$$\nu_{FSR} = \frac{1}{2n_o \ell_o}$$

m	= ETALON PASSBAND ORDER
$\delta\nu$	= ETALON BANDWIDTH
ν_{FSR}	= FREE SPECTRAL RANGE
F	= FINESS
n_o	= INDEX OF REFRACTION BETWEEN PLATES
l_o	= PLATE SEPARATION

FIGURE 19.

FABRY PEROT ETALON (FPE) RESPONSE CHARACTERISTICS

A block diagram of a basic FPE configuration for high spectral resolution measurements is shown in Figure 20. As shown, it consists of a dielectric interference filter followed by several etalon filters each with a decreasing free-spectral range. Figure 20b shows single line output with an idealized bandpass response of the dielectric filter. To that end, the free spectral range (FSR) of the first etalon is made equal or greater than the width of the interference filter, so as to assure a single order bandpass response within the filter bandwidth (see Figure 20c). The ultimate high spectral resolution is obtained from consecutive etalons, each having its FSR equal to the bandwidth of the preceding etalon as shown in Figures 20d and 20e. The number of required FPE stages in the configuration is a function of the achievable finesse for a desired spectral resolution.

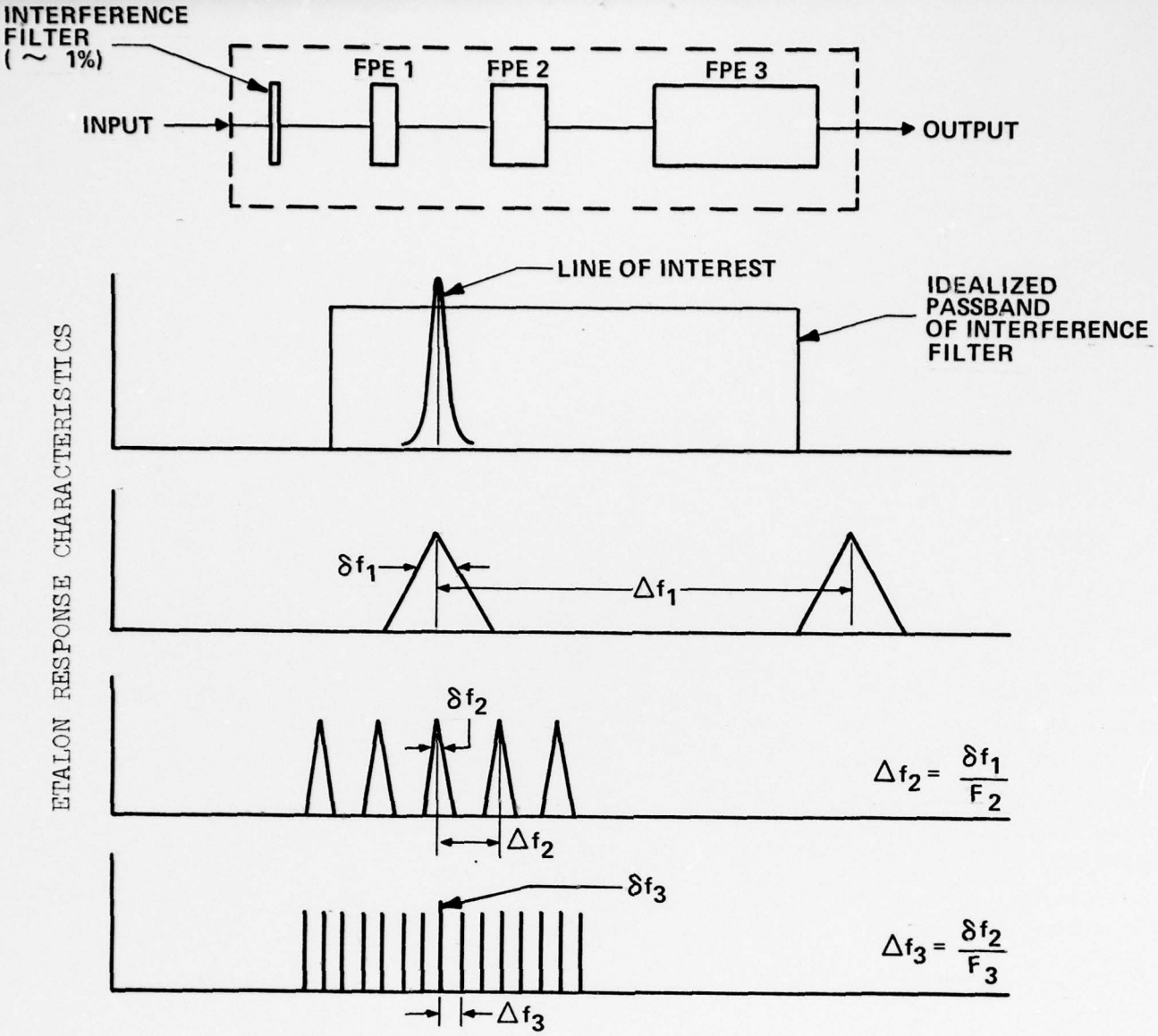

FIGURE 20.

PROPOSED BASIC SPECTROSCOPIC INSTRUMENTATION

7.0 REFERENCES

1. J.W. Walters, K.F. Kunzi, R.L. Pettyjohn, R.K.L. Poon and D.H. Staelin, "Remote Sensing of Altitude Temperature Profiles With the Nimbus 5 Microwave Spectrometer," Journal of Atmospheric Sciences, Vol. 32, pp 1953-1969, Oct. 1975.
2. R.K. Seals and B.J. Peyton, "Remote Sensing of Atmospheric Pollutant Gases Using an Infrared Heterodyne Spectrometer," Proceedings of the International Conference on Environmental Sensing and Assessment, Vol. 1, p 10-4, Las Vegas, Nevada, Sept. 1975.
3. Barney J. Conrath, "Vertical Resolution of Temperature Profiles Obtained From Remote Radiation Measurements," J. of the Atmospheric Sciences, Vol. 25, Oct. 1972.
4. Handbook of Geophysics and Space Environment, Air Force Cambridge Research Laboratories, McGraw-Hill Book Co.
5. W.L. Smith, "Iterative Solution of the Radiative Transfer Equation for the Temperature and Absorbing Gas Profile of an Atmosphere," Applied Optics, Vol. 9, No. 9, Sept. 1970.
6. M.T. Chahine, "Inverse Problem in Radiative Transfer: Determination of Atmospheric Parameters," J. of the Atmospheric Sciences, Vol. 27, Sept. 1970.
7. R.A. McClatchey, "AFCRL Atmospheric Absorption Line Parameters Compilation," Environmental Research Papers, No. 434, Air Force Systems Command, L.G. Hanscom Field, Bedford, Mass.

DISTRIBUTION LIST

Scientific Officer
DODAAD Code N00014

Administrative Contracting
Officer
DODAAD Code S3309A

Director, Naval Research (6)
Laboratory
Code 2627
Washington, D.C. 20375

Office of Naval Research (6)
Department of the Navy
Code 102IP
Arlington, Va. 22217

Defense Documentation Center (12)
Bldg. 5, Cameron Station
DODAAD Code S47031
Alexandria, Va. 22314

Office of Naval Research Branch
Office - Boston
DODAAD Code N62879
495 Summer Street
Boston, Mass. 02210

Dr. Alex Shlanta
Naval Weapons Center
Code 3173
China Lake, Ca. 93555

Peter Yu
Naval Weapons Center
Code 3173
China Lake, Ca. 93555

Jay Rosenthal
PMTC
Code 3253
Point Mugu, Ca. 93042

LT Arthur W. Green
FCTCP
Code 32
200 Cataline Blvd.
San Diego, Ca. 92147

David J. Reed
PMTC
Code 3143
Point Mugu, Ca. 93042

David Kwan
MIT/Lincoln Lab.
Lexington, Mass. 02173

CWO2 Lance Kruse
NAVWEASERVFAC
San Diego, Ca. 92135

Bill Heile
Naval Avionics Facility
Code 812
Indianapolis, In. 46218

Jim Placke
Naval Avionics Facility
Code 945
Indianapolis, In. 46218

Commanding Officer
Naval Environmental Prediction
Research Facility, Monterey, Ca.

Dr. Murray Schefer
Naval Air Systems Command
Code 370
Washington, D.C. 20360

Dr. L. Ruhnke
Naval Research Laboratory
Code 8320
Washington, D.C. 20375

Dr. B. Katz
Naval Surface Weapons Center
Code WR42
White Oak, Md. 20910

Office of Naval Research
Code 421
Arlington, Va. 22217